

Collapse of Eurasian ice sheets 14,600 years ago was a major source of global Meltwater Pulse 1a

Jo Brendryen^{1,2,3,*}, Hafliði Haflidason^{1,2}, Yusuke Yokoyama⁴,
Kristian Agasøster Haaga^{1,2,3}, and Bjarte Hannisdal^{1,2,3}

¹*Department of Earth Science, University of Bergen, Norway*

²*Bjerknes Centre for Climate Research, University of Bergen*

³*K.G. Jebsen Centre for Deep Sea Research, University of Bergen*

⁴*Atmosphere and Ocean Research Institute, University of Tokyo, Japan*

*Corresponding author: jo.brendryen@uib.no

Rapid sea-level rise caused by the collapse of large ice sheets is a global threat to human societies¹. In the last deglacial period, the rate of global sea-level rise peaked at more than 4 cm/yr during Meltwater Pulse 1a, which coincided with the abrupt Bølling warming event ~14,650 yr ago²⁻⁵. However, the sources of the meltwater have proven elusive^{6,7}, and the contribution from Eurasian ice sheets has until now been considered negligible⁸⁻¹⁰. Here we show that marine-based sectors of the Eurasian ice sheet complex collapsed at the Bølling transition and lost an ice volume of between 4.5 and 7.9 m sea level equivalents (95% quantiles) over 500 yr. During peak melting 14,650 - 14,310 yr ago, Eurasian ice sheets lost between 3.3 and 6.7 m sea level equivalents (95% quantiles), thus contributing significantly to Meltwater Pulse 1a. A mean meltwater flux of 0.2 Sv over 300 yr was injected into the Norwegian Sea and the Arctic Ocean during a time when proxy evidence suggests vigorous Atlantic meridional overturning circulation^{11,12}. Our reconstruction of the EIS deglaciation shows that a marine-based ice sheet comparable in size to the West Antarctic ice sheet can collapse in as little as 300-500 years.

Understanding the response of marine-based ice sheets to global warming is critical to future sea-level projections¹. Today large marine-based ice sheets are situated in the Antarctic, with the West Antarctic ice sheet long considered to be particularly vulnerable¹³⁻¹⁶. The time scale and magnitude of its potential disintegration are highly uncertain, however, and its projected contribution to sea-level rise over the next centuries varies by orders of magnitude^{17,18}. To add further empirical constraints, researchers turn to past deglaciation events to study the tempo and mode of ice sheet collapse in a warming world. The West Antarctic ice sheet itself survived the end of the last ice age, but an important analogue can be found in the collapse of the Late Pleistocene Eurasian ice sheet complex (EIS) (Fig. 1).

During the last glacial maximum, 20-21 kyr ago, the EIS attained a maximum ice volume of ~24 m global sea level equivalents (SLE)¹⁹, including large marine-based sectors extending all the way to the continental shelf edge. These sectors formed an extensive interface to the Arctic Ocean and the Nordic Seas, which are one of the main loci of deep-water formation essential to the Atlantic Meridional Overturning Circulation (AMOC). This region is thus of particular importance for understanding the impact of meltwater forcing on ocean circulation and global climate²⁰.

At the end of the last ice age, abrupt Northern Hemisphere warming at the Bølling transition ~14,650 yr BP coincided with accelerated melting of ice sheets in an event known as global Meltwater Pulse 1a (MWP-1a)²⁻⁵. During this event, mean global sea-level rose by 12-14 m in ~340 yr, at a rate of at least 4 cm/yr⁵. The sources, magnitude and timing of the MWP-1a have been a subject of controversy over the past decades, and a significant role for the EIS has until now been largely dismissed^{6,8,10}. Previous reconstructions of the EIS deglaciation and meltwater contributions^{8,19,21} have concluded that the bulk of the marine sectors were deglaciated well before the Bølling transition and the MWP-1a. These reconstructions have, however, assumed a constant marine radiocarbon reservoir age (R) similar to the modern value throughout the deglaciation, typically around 400 yr. Although the uncertainty of this assumption is commonly acknowledged, a lack of constraints on the temporal evolution of R in the Norwegian Sea has prevented a more accurate reconstruction of the deglaciation.

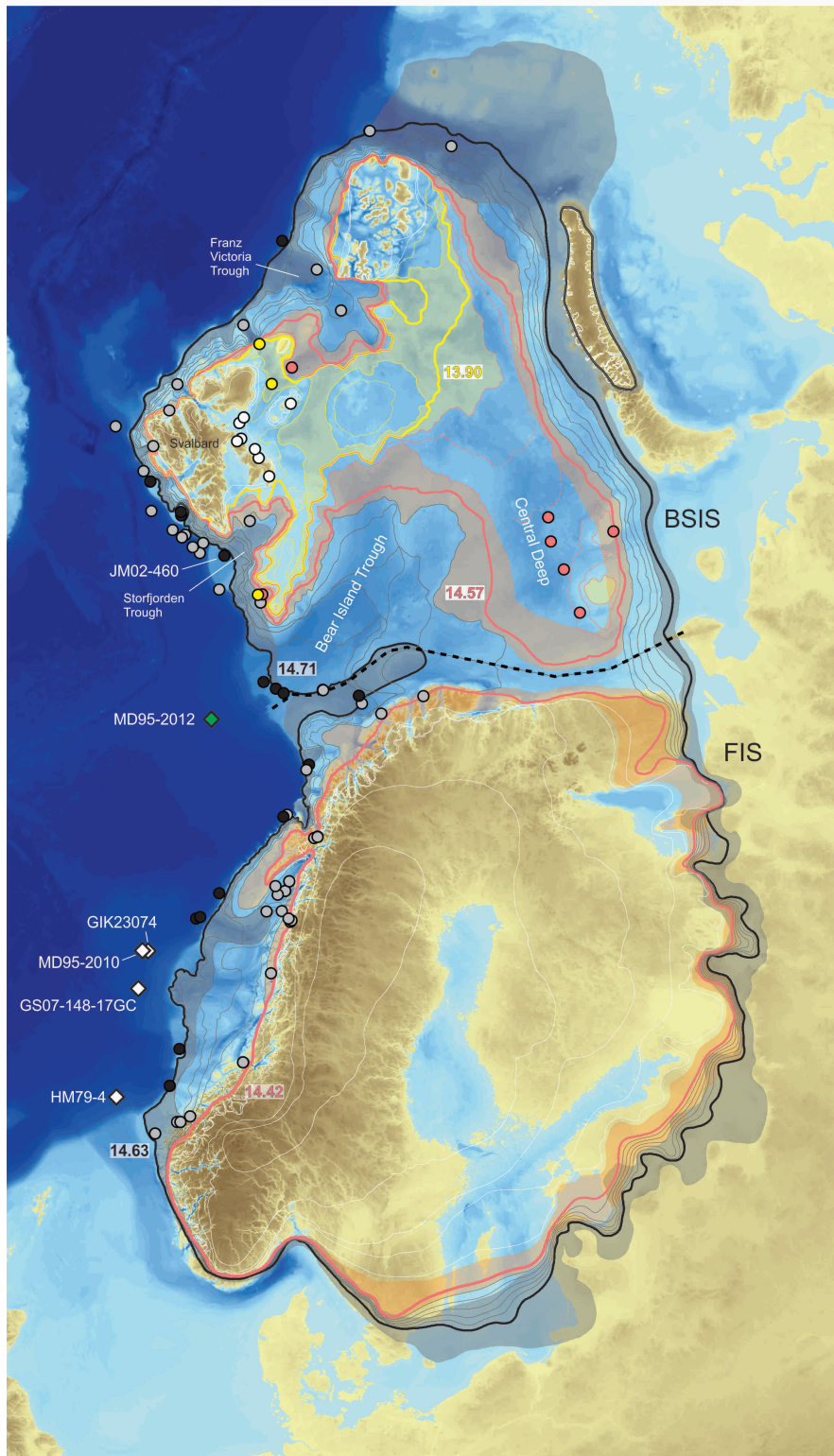


Figure 1: Reconstructed Late Pleistocene EIS complex comprised of the Fennoscandian Ice Sheet (FIS) and the Barents-Svalbard Ice Sheet (BSIS). Contour lines represent ice margins at different stages of the deglaciation. Thick lines represent ice margin positions at boundaries between the deglacial phases used in the Bayesian chronology (Supplementary Data Fig. 7 and 8 and Supplementary Data File). Black lines are the inferred ice margin following the late Heinrich Stadial 1 ice advance. Pink lines are the ice margins that followed the separation of the BSIS and FIS. Yellow lines mark ice margins when the BSIS are constrained on the archipelagos and shallow banks in the northern Barents sea. The median age of each margin is indicated. The accompanying transparent fields mark the geographic uncertainties associated with the respective ice margins. Thin lines mark the suggested ice sheet retreat pattern within each phase as synthesized from the literature listed in [Methods](#). The black stippled line marks the separation between the FIS and the BSIS used in the area-volume calculation when they were confluent. Black filled circles mark sites used to constrain the Heinrich Stadial 1 extent of the ice sheet. The positions of the stratigraphic records and dates used to constrain the deglacial phases are marked with gray, pink, yellow and white filled circles. White diamonds mark the position of cores used to reconstruct the Norwegian Sea ^{14}C reservoir age. White lines indicate ice margins adopted from the Dated-1 reconstruction.

48 Norwegian Sea ^{14}C reconstruction and deglacial chronology

49 We here present a new chronology for the deglaciation of the marine-based sectors of the EIS complex,
50 using new constraints on the Norwegian Sea ^{14}C and R to calibrate marine ^{14}C dates linked to the retreat
51 of the EIS. We take advantage of the close connection between North Atlantic climate and the Asian Mon-
52 soon²²⁻²⁶ to align Norwegian Sea paleoceanographic records with a U/Th-dated speleothem record from
53 Hulu Cave, China^{27,28} (Fig. 2; Methods; Supplementary Fig. 1). This alignment is corroborated by a
54 tephrochronological marker bed found both in Norwegian Sea sediments and Greenland ice cores (Supple-
55 mentary Fig. 1, Methods). The age difference between 99 ^{14}C dates compiled from these same cores and
56 the corresponding atmospheric ^{14}C age represented by the IntCal13 calibration curve²⁹ (Fig. 2F) yields a
57 new and detailed account of the temporal evolution of the Norwegian Sea ^{14}C reservoir age from 19,000 to
58 12,500 yr BP (Fig. 2G).

59 Prior to the Bølling warming, the Norwegian Sea had a mean R of 1,620 ^{14}C yr (Fig. 2G). Then, at the
60 Bølling transition, R abruptly declined by $\sim 1,500$ ^{14}C yr in less than 400 calendar yr and the mean R for the
61 remainder of the warm period was 420 ^{14}C yr (Fig. 2). We resample (Methods) the compiled timeseries of
62 ^{14}C ages by a Monte Carlo technique where chronological, stratigraphical and ^{14}C uncertainties are taken
63 into account (Fig. 2F) and use this to calibrate published conventional radiocarbon ages from sedimentary
64 archives that are linked to the dynamics and deglaciation of marine-based sectors of the EIS. The deglacia-
65 tion of the EIS complex is reconstructed using a probabilistic approach, taking into account uncertainty in
66 both area and age (Methods). The resulting estimates are reported here as medians and 95% quantiles from
67 the probability distributions. The deglaciation for the BSIS and FIS is constrained independently, yielding
68 a sequence of reconstructed ice margins with uncertainty bounds (Fig. 1).

69 Our revised EIS chronology (Supplementary Figs. 7 and 8; Supplementary Data File) suggests that
70 the Barents-Svalbard ice sheet (BSIS) remained in an advanced position until 14.71 (14.81-14.63) kyr cal
71 BP, after which it rapidly retreated from the outer shelf and deeper troughs at the Bølling transition. At
72 14.57 (14.67-14.46) kyr cal BP, the BSIS had separated from the Fennoscandian ice sheet, forming an
73 ice lobe over the Central Deep in the Barents Sea, and by 13.90 (14.20-13.57) kyr cal BP it had become
74 confined to islands and shallow banks in the northern Barents Sea (Fig. 1). The reconstructed retreat of the
75 BSIS is congruent with a prominent early Bølling meltwater $\delta^{18}\text{O}$ anomaly observed in proxy records from
76 core MD95-2012 retrieved from the Barents Sea margin^{35,36}. Deglaciation of the Fennoscandian ice sheet
77 commenced at 14.63 (14.78-14.49) kyr cal BP, and by 14.42 (14.57-14.20) kyr cal BP it had retreated from
78 the continental shelf into the coastal areas (Fig. 1).

79 EIS collapse and MWP-1a contribution

80 Based on the area-volume relationship for extant ice sheets³⁷, our reconstruction implies that before the
81 Bølling transition, the EIS contained an ice volume of 15.0 (13.9-16.1) m SLE (Figure 2H). We also applied
82 an alternative area-volume regression using the output of a transient model of the EIS complex itself³⁸
83 (Supplementary Fig. 9). Although the alternative regression yields an EIS volume that is 2.7 m SLE less
84 than the Paterson approximation at the start of the deglaciation, the estimated ice loss between 14.7 and
85 14.4 kyr BP differs by only ~ 0.2 m SLE, which is negligible with respect to our conclusions. Hence, our
86 mass loss estimates are robust to the assumptions of the area-volume conversion (Supplementary Fig. 9).

87 Our new reconstruction implies that the marine-based EIS collapsed at the Bølling transition. Over
88 a 500 yr period, starting at 14.71 cal kyr BP, the EIS lost a volume of 6.2 (4.5-7.9) m SLE. Within the
89 MWP-1a time span as defined by the Tahiti chronology (14.65-14.31 kyr BP)⁵, the EIS lost a volume of
90 4.9 (3.3-6.7) m SLE, implying that the collapse of the EIS was a major source of the MWP-1a. Given the
91 presence of ichnofabric in parts of the Norwegian Sea core sediments, we show that bioturbation would
92 result in the smearing out of a more abrupt change in the reservoir age occurring close to the Bølling
93 transition, effectively shifting the start of the R decline back in time by more than 200 calendar years
94 (Methods; Supplementary Fig. 6). Therefore, our mass loss estimates are likely to be conservative, in the
95 sense that they may overestimate the time span of the EIS collapse and thus underestimate its contribution
96 to the MWP-1a.

97 Implications for deglaciation and ice sheet collapse

98 An EIS contribution of 4.9 (3.3-6.7) m SLE to the MWP-1a is substantially larger than previous estimates
99 in Dated-1¹⁹ (1.1 m SLE when interpolated to 340 yr from the most-credible Dated-1 ice margins at 15

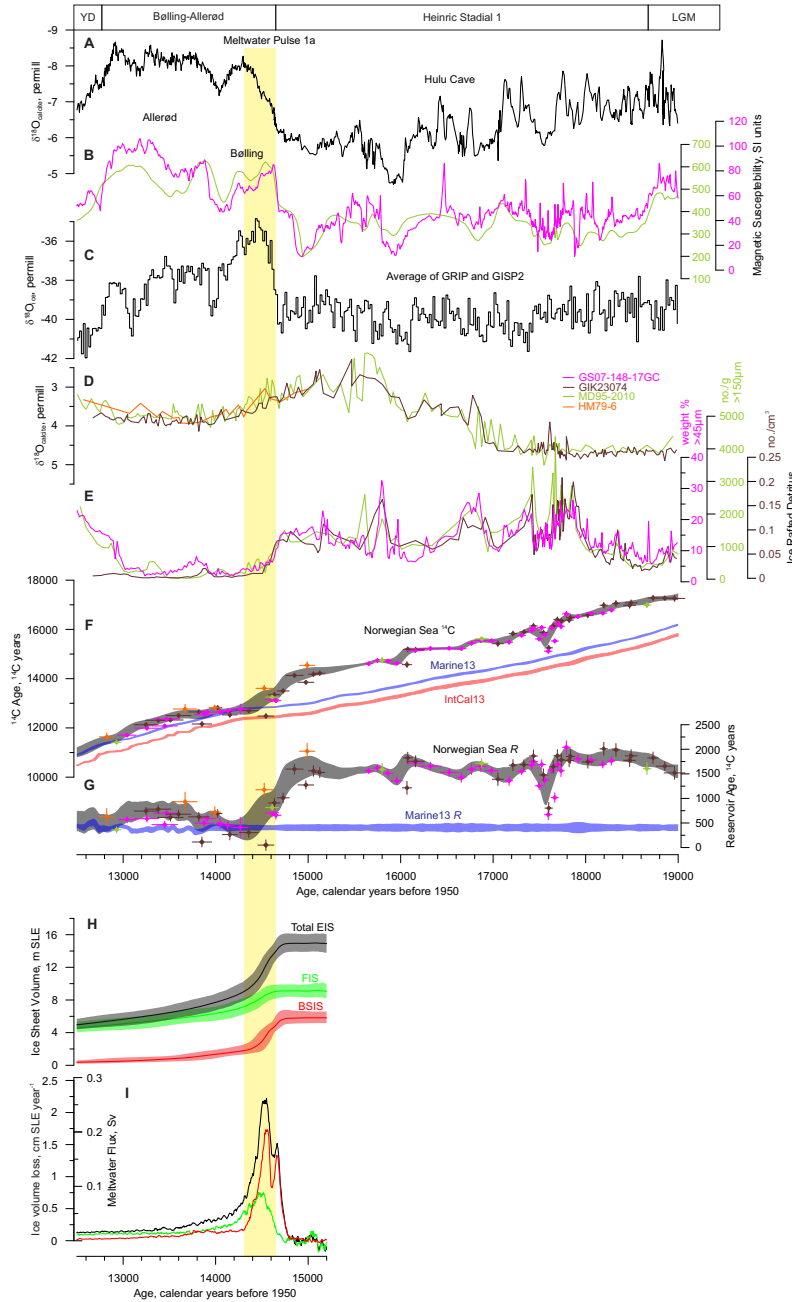


Figure 2: Records of climate, ice volume and meltwater flux from the Eurasian Ice Sheet complex. **A**, $\delta^{18}\text{O}$ record from Hulu cave speleothem H82. **B**, Magnetic susceptibility from two Norwegian sea sediment cores (Fig. 1), aligned with the speleothem $\delta^{18}\text{O}$ record in **(A)**. **C**, Average $\delta^{18}\text{O}$ record from Greenland summit ice cores (GISP2 and GRIP) on the GICC05 chronology. **D**, Planktonic foraminifera $\delta^{18}\text{O}$ (*Neoglobigerina pachyderma* sinistral) from three Norwegian Sea sediment cores. **E**, Proxy records of ice rafted detritus from Norwegian Sea cores. **F**, Compiled AMS ^{14}C ages from Norwegian Sea sediment cores (GS07-148-17GC, this study; GIK23074; MD95-2010; HM79-6). Horizontal error bars represent the 68.2% quantiles (equivalent to 1σ) of the GS07-148-17GC deposition model. Gray shading represents $\pm 1\sigma$ of the Monte Carlo sampling of the probability density functions of both the stratigraphic and chronological core alignments and the ^{14}C uncertainty. **G**, Norwegian Sea ^{14}C reservoir age, R is calculated as the difference between the conventional ^{14}C ages (at the median age) and the IntCal13 atmospheric ^{14}C curve. Vertical error bars are the root sum of squares of the ^{14}C uncertainties. The average global reservoir age represented by the Marine13 calibration curve is plotted for reference. **H**, Reconstructed ice volume for the Eurasian Ice Sheet (EIS) complex expressed as sea level equivalents (SLE; 25 yr running mean of median and 95% quantiles). FIS: Fennoscandian Ice Sheet; BSIS: Barents-Svalbard Ice Sheet. **I**, median rate of ice volume loss in cm SLE per yr and as meltwater flux (Sv) (colors as in **(H)**).

and 14 kyr BP), and is comparable to the estimated contribution from the much larger North American ice sheet (5-6 m SLE in ref. ³⁹, 6.4-9 m SLE (interpolated to 340 yr) in ref. ⁴⁰, and 4-7 m SLE in ref. ¹⁰). Although a prominent MWP-1a contribution from the EIS is consistent with observed sea-level fingerprints ⁹, the inferred total amplitude of the MWP-1a and the distribution of other meltwater sources need to be reconsidered in light of our findings ^{5,6}.

Observed records of relative sea-level fall in Scotland do not support the predicted sea-level fingerprints from a glacio-isostatic model of the MWP-1a when sourced solely from the Laurentide ice sheet and Antarctica, but this discrepancy may be reconciled by a larger meltwater contribution from the EIS ⁴¹. A large EIS contribution is also consistent with near-field records from both western and northern Norway that show falling relative sea-level during the Bølling ⁴²⁻⁴⁴, as expected if gravitational and isostatic effects from EIS mass loss overwhelmed eustatic sea-level rise from the MWP-1a.

Modeled far-field sea-level fingerprints suggest that a MWP-1a sourced from the EIS would increase the local sea-level by about 10% at Tahiti and by 4% at the Sunda shelf ⁹. This proportional increase would translate our conservative estimates of EIS mass loss during the MWP-1a into 3.6-7.4 m relative sea level rise at Tahiti and 3.3-7.0 m at the Sunda shelf. If we consider the observed low-end local sea-level rise of 12 m at Tahiti ⁵, then our results suggest that the EIS collapse may have contributed 30-60% of the MWP-1a

116 at this locality. For the high-end local sea level rise estimate of 17.3 m at the Sunda shelf⁶, our mass loss
117 estimates correspond to 20-40% of the local sea level rise. A more accurate estimate of the eustatic sea-
118 level contribution from the EIS collapse will require additional constraints on the effect of glacio-isostasy
119 and ice volume below flotation. Nevertheless, our findings provide strong empirical evidence that the EIS
120 was a major source of the MWP-1a. Combined with recent estimates for the North American Ice Sheet
121 MWP-1a contribution^{10,40} our EIS mass loss estimates are sufficient for explaining the far-field relative sea
122 level observations without a major Antarctic contribution, consistent with the lack of field evidence for a
123 large retreat of the Antarctic Ice Sheet⁴⁵.

124 Our new account of the EIS collapse is an important step towards solving the mysteries of the Bølling
125 event and the MWP-1a, which also raises a number of research questions pertinent to climate change sce-
126 narios for the near future.

127 (1) What triggered the collapse of the marine-based EIS? In addition to the abrupt atmospheric and
128 surface ocean warming at the Bølling transition^{32,46,47}, proxy records from core JM02-460 suggest a marked
129 subsurface warming on the Barents Sea continental shelf during the late Heinrich Stadial 1⁴⁸, close to the
130 inferred ice sheet grounding line (Fig. 1). A vast ice-ocean interface rendered marine-based EIS sectors
131 potentially very sensitive to subsurface warming and melting at the grounding line, which is considered to
132 be one of the main drivers of current^{49,50} and past⁵¹ mass loss from the Antarctic ice sheets.

133 (2) Which mechanisms drove the rapid EIS retreat? In addition to surface melting and the likely in-
134 volvement of mass-balance/elevation feedback³⁹, continuity between subglacially carved lineations and
135 iceberg ploughmarks in the Bear Island Trough suggests calving of deep-keeled icebergs at the ice front⁵².
136 These findings are consistent with the operation of the marine ice cliff instability mechanism (MICI)^{53,54}
137 during the rapid ice sheet retreat. The current water depth in the SW Barents Sea is 400-500 m, less than
138 the ~800 m thought to be required by MICI⁵³. Isostatic depression by ice sheet loading⁵⁵, however, may
139 have lowered the bed sufficiently for this mechanism to operate. Alternatively, the MICI may operate at
140 shallower depths than currently parameterized in models. Although past Antarctic deglaciation events can
141 be explained without invoking this specific mechanism⁵⁶, the MICI is featured in the model yielding the
142 high-end future rate of ice loss from the Antarctic Ice Sheet¹⁸.

143 (3) What was the impact of EIS meltwater on ocean circulation? We estimate that a meltwater flux of
144 0.2 Sv over 300 yr was injected into the Norwegian Sea and the Arctic Ocean during the early Bølling, a
145 time period when proxy evidence suggests vigorous Atlantic meridional overturning circulation^{11,12,57}. This
146 result implies that the relationship between freshwater injection and North Atlantic deep water formation is
147 not clear-cut, and highlights the need to resolve meltwater routing⁵⁸.

148 Our reconstruction of the EIS deglaciation shows that an ice sheet comparable in size to the West
149 Antarctic ice sheet can collapse in as little as 300-500 years. Ice sheet models used to predict the future of
150 marine-based Antarctic ice sheets differ markedly in their predicted rates of ice loss and in the mechanisms
151 involved^{17,18}. We provide new empirical constraints that raise the prospect of using the marine-based EIS
152 collapse as a benchmark for validating such ice sheet models and ultimately improve projections of future
153 sea-level rise. The estimated rates of ice loss from the EIS during the early Bølling (~1.6 cm SLE yr⁻¹
154 averaged over 300 yr, peaking at ~2.2 cm SLE yr⁻¹) are comparable to high-end values of mass loss
155 projected for the West Antarctic ice sheet in the next centuries.

156 **Methods**

157 **Temporal evolution of the marine radiocarbon reservoir age (*R*)**

158 We compiled a time series of 41 new and 58 previously published AMS ¹⁴C ages of the polar subsurface-
159 dwelling planktonic foraminifer *Neoglobigerina pachyderma* sinistral, from four Norwegian Sea sediment
160 cores (Fig. 2).

161 Sediments from core GS07-148-17GC were continuously sampled in 0.5 cm thick slices that were dried
162 and washed over 45 and 100 μm sieves. From the >100 μm grain size fraction, 47 samples of monospecific
163 *Neoglobigerina pachyderma* (sinistral) were picked and measured for ¹⁴C at the Atmosphere and Ocean
164 Research Institute (AORI) at the University of Tokyo. Foraminiferal tests were weighed and washed ultra-
165 sonically before converting them into graphite under the protocol described in⁵⁹. For samples smaller than
166 0.3 mgC, a specially designed high vacuum line was used for the preparation⁶⁰. Target graphite was then
167 measured by the single stage accelerator mass spectrometer at AORI⁶¹.

168 The ¹⁴C data and other records from three of the cores (MD95-2010, HM79-6 and GIK23074) are
169 previously published³¹⁻³⁴. These cores were stratigraphically aligned to core GS07-148-17GC using tie-
170 points defined by a combination of records of ice rafted detritus (IRD), magnetic susceptibility (MS) and the

171 $\delta^{18}\text{O}$ and $\delta^{13}\text{C}$ of *N. pachyderma* sinistral (Supplementary Fig. 4). The alignment to the GS07-148-17GC
172 depth scale was performed with the Oxcal v4.3.2 software⁶², using the P_Sequence sediment deposition
173 model⁶³ and the variable k option⁶⁴. We assume an uncertainty of ± 2 cm (1σ) for each tie-point.

174 Absolute age control of the core records including ^{14}C was obtained by event-stratigraphic correlation
175 with the U/Th dated H82 speleothem $\delta^{18}\text{O}$ record from Hulu Cave, China²⁷ and isotope records from
176 Greenland Summit ice cores³⁰ (Supplementary Fig. 1). The rationale for this correlation rests on the close
177 relationship between Greenland temperatures, North Atlantic Ocean temperature and circulation, and the
178 Asian Monsoon on decadal to millennial time scales^{22–25}.

179 For the correlation we used the MS record of core GS07-148-17GC determined in 2 mm steps by a
180 GeotekTM multi sensor core logger and a Barlington2 point sensor. MS in Norwegian Sea sediments is
181 considered to be a proxy for the strength of the warm Atlantic Water inflow over the basaltic Iceland Scot-
182 land Ridge through ocean current erosion and transport of magnetic mineral grains that are subsequently
183 deposited in the S-Norwegian sea; the Atlantic water inflow is in turn tightly linked to the general North
184 Atlantic climate, including Greenland temperatures^{33,65–67}.

185 We used the Hulu cave speleothem H82 $\delta^{18}\text{O}$ record as the Norwegian Sea MS correlation target be-
186 cause of its high temporal resolution, and because it contains high-amplitude signals that covary with the
187 MS record. This covariance has been attributed to fast atmospheric teleconnections between ocean circula-
188 tion in the North Atlantic and regional Asian monsoon intensity and isotopic fractionation captured in
189 the speleothem $\delta^{18}\text{O}$ ^{23,68}. The covariation between Greenland ice core $\delta^{18}\text{O}$ and Norwegian sea MS is
190 more subdued, especially during Heinrich Stadial 1 (HS1), which has been attributed to a diminishing ef-
191 fect of North Atlantic circulation on Greenland temperatures during cold intervals⁶⁹. The Hulu Cave H82
192 chronology rests solidly on a large number of U/Th dates that, paired with AMS ^{14}C measurements, yield
193 a high-resolution time series of atmospheric ^{14}C ages²⁷, which forms the backbone of the IntCal13 atmo-
194 spheric radiocarbon reconstruction²⁹. By tying our Norwegian Sea ^{14}C record directly to the Hulu Cave
195 $\delta^{18}\text{O}$, we operate on the same absolute time scale as IntCal13. Hence, we can determine the reservoir age
196 effect in the Norwegian Sea (the difference between the IntCal13 atmospheric ^{14}C ages and the Norwegian
197 Sea ^{14}C ages). This approach is more precise than tying the Norwegian Sea record to the Greenland ice
198 core chronology (GICC05)⁷⁰, which has a cumulative counting error of up to ± 400 yr in the time interval
199 considered here.

200 The GS07-148-17GC age model was constructed using the Oxcal v4.3.2 software⁶², and the P_Sequence
201 sediment deposition model⁶³ with the variable k option⁶⁴. The age-uncertainty for each tie-point was de-
202 rived from a Oxcal P_Sequence model of the H82 speleothem, using the U/Th dates from Ref.²⁷ (Supple-
203 mentary Fig. 1). To account for uncertainty in the lead-lag relationships between the records, we assume
204 an added uncertainty of ± 25 yr (1σ) to each tie-point. Although the correlation depicted in Supplementary
205 Fig. 1 is very detailed, the resulting age-depth relationship for the Norwegian Sea cores remains smooth
206 and roughly linear between the Holocene boundary and an interval of rapid deposition centered at 17.5 ka
207 that is related to the break-up of the Norwegian Channel Ice Stream^{71,72} and a catastrophic drainage of a
208 large ice dammed lake in the North Sea⁷³. Our correlation is validated by the occurrence of the Vedde Ash
209 layer in the interval ascribed to Younger Dryas both in the GS07-148-17GC and in the Greenland ice core
210 records³⁰ (Supplementary Fig. 1).

211 To assess the sensitivity of our results to the reconstructed chronology, we explored an alternative depo-
212 sition model without any assumptions of teleconnections or synchrony between proxy records (Supplemen-
213 tary Fig. 2). We constrained the ages of this alternative model with the Vedde Ash, which is dated by layer
214 counting in the Greenland ice cores to 12121 ± 57 cal yr BP on the GICC05 chronology⁷⁴ (Supplementary
215 Fig. 1), and with 24 ^{14}C dates from our compilation (Supplementary data file). We restricted the use of
216 ^{14}C dates to the Younger Dryas and Bølling-Allerød time periods where the Norwegian Sea R has been
217 independently constrained by paired marine and terrestrial ^{14}C dates⁷⁵. We then used the *Marine13* cali-
218 bration curve²⁹ with a ΔR of 100 ± 50 yr, and the same depositional model as in our preferred chronology,
219 invoking the default *general* outlier model⁷⁶. Due to a lack of pre-Bølling age constraints, this alterna-
220 tive chronology expectedly shows much greater pre-Bølling age uncertainty than our preferred chronology.
221 Nevertheless, the two chronologies overlap almost entirely in their 68.2 % (1σ) credible intervals (Supple-
222 mentary Fig. 2). Notably, the alternative chronology yields a drop in ^{14}C age at the Bølling transition that is
223 steeper than in our preferred chronology, implying an even more abrupt EIS collapse. Hence, we conclude
224 that the inferred drop in R at the Bølling transition is unlikely to be an artefact of the age model, and that
225 our estimates are conservative in terms of the rate of EIS mass loss and its contribution to the MWP-1a.

226 From the compiled time series of ^{14}C ages we calculate R as the difference between the Norwegian Sea
227 ^{14}C and the *Intcal13* atmospheric ^{14}C calibration curve²⁹ (Fig. 2F). To incorporate the uncertainty in both
228 calendar ages and ^{14}C ages in our reconstructed ^{14}C and R record, we generated an uncertainty envelope

229 by Monte Carlo sampling of multiple posterior probability density functions (PDFs) generated by the Oxcal
230 sediment deposition models of the core stratigraphies: (i) PDFs of the stratigraphic alignment of the four
231 Norwegian Sea sediment cores, (ii) PDFs of the depositional model for the GS07-148-17GC core, which
232 incorporate both the uncertainty in the Hulu Cave target $\delta^{18}\text{O}$ record and uncertainty in the correlation to
233 the Hulu Cave record, and (iii) PDFs of the ^{14}C measurements. Our time series of ^{14}C ages is the mean
234 $\pm 1\sigma$ of 10^5 Monte Carlo realizations of the dataset in 10-yr bins using linear interpolation. It spans the
235 period from 12,200 to 19,000 cal yr BP and is available as supplementary data formatted as a .14c file that
236 can be used directly in radiocarbon calibration software.

237 Our R record are consistent with R values previously reported from the North Atlantic and the Norwe-
238 gian Sea and coast^{34,75,77–79}. Although a different approach was used to constrain the calendar ages of core
239 GIK23074³⁴, we arrive at similar reservoir ages.

240 Tephrochronology

241 Tephra shards were quantified in the $>100\ \mu\text{m}$ grain fraction in ~ 20 cm interval of core GS07-148-17GC
242 corresponding to the Younger Dryas chronozone. This interval was chosen with the aim of finding the
243 Vedde Ash tephra that is a key chronostratigraphic marker horizon in the North Atlantic region, and is also
244 found in the Greenland Ice cores³⁰ and several of the Norwegian Sea cores used in this study^{32,33}. Based on
245 their colour and morphological character, tephra particles were grouped into a transparent-white rhyolitic
246 type of tephra and a brown basaltic type of tephra. The total count from each of these tephra types was
247 normalized using the total dry weight of the samples and the results plotted versus depth (Supplementary
248 Fig. 1)

249 Tephra shards from three depth intervals (32.5-33.0, 33.5-34.0 and 36.0-36.5 cm) were selected for geo-
250 chemical analysis. 25-30 shards of both rhyolitic and basaltic type were picked for major oxide geochemical
251 analysis on the University of Bergen Zeiss Supra 55 VP scanning electron microscope. The microscope was
252 attached to a Thermo energy dispersive X-ray spectrometer with 9.5 mm working distance, beam current
253 of 1.00 mA, an aperture size of $60\ \mu\text{m}$, beam width of $6\ \mu\text{m}$ and detection time of 60 s. The results are
254 presented in the Supplementary Data File and in Supplementary Fig. 3. As the geochemical analysis were
255 performed directly on the shards and without any leveling or polishing the beam will hit the surface from
256 different angles. This resulted in that the counting rate of the different elements becomes slightly more
257 scattered than during analysis on a polished thin section. The major element composition is, however,
258 consistent with published major element data from the Vedde Ash (Supplementary Fig. 3).

259 Ice sheet margin reconstructions

260 We reconstructed the deglaciation of the EIS complex in a Bayesian chronological framework using Oxcal
261 4.2.4^{62–64,76}. The prior model was constructed using available chronological, stratigraphical and morpho-
262 logical data that were aggregated, independently for the BSIS and the FIS, into a sequence of phases with
263 known relative ages. A phase in this context refers to the retreat (or advance) of the ice sheet in a specific
264 area.

265 We grouped the deglaciation of the FIS ice sheet into two phases: (i) late HS1 advance and (ii) deglacia-
266 tion on the continental shelf and outer coasts. Following the deglaciation of the continental shelf, we use the
267 ages and ice sheet geometries provided by the *Dated-1* reconstruction¹⁹ in the 14-10 ka interval, as these
268 are predominantly based on terrestrial dates not affected by our recalibration of the marine ^{14}C dates. The
269 ice margins along the southern and eastern margins of the FIS were generated by interpolating between the
270 15 ka and 14 ka *Dated-1* ice margins using the TopoToRaster tool in ArcMap 10.5.1. On the Norwegian
271 continental shelf, evidence suggests that the deeper troughs deglaciated rapidly compared to the shallower
272 banks^{80–82}.

273 The more complex deglaciation history of the BSIS was divided into five phases: (i) late HS1 advance,
274 (ii) deglaciation of the major overdeepened areas of Storfjorden trough, Bear Island trough and Franz Vic-
275 toria trough, and the narrow continental shelf areas west and north of Svalbard, (iii) deglaciation of the
276 Central Deep, (iv) final deglaciation of the shallow banks in the northern Barents Sea, and (v) ice retreat
277 to the Svalbard archipelago. An early deglacial phase was added before the late HS1 advance, without
278 assigning ice sheet margins. At 12-10 ka we used the *Dated-1*¹⁹ BSIS ice sheet geometries.

279 We adapt a previously proposed ice sheet retreat pattern for the southern Barents Sea, suggesting
280 episodic rapid retreat in the Bear Island trough^{83–87}. Well preserved retreat ridges suggest that the ice
281 remaining on the shallower banks retreated more slowly⁸⁵. The final ice movement on the southern Barents

282 sea banks was from the east^{85,87} suggesting an ice dome remained over the Central Deep following the
283 separation of the BSIS and the FIS (Fig. 1).

284 The age-control of each phase was constrained by the ages of sediment facies and/or facies transitions
285 linked to ice margin positions within the phase (Supplementary Figs. 7 and 8), as well as by the age
286 information of adjacent phases in the sequence. We used the published ¹⁴C dates either directly as ages of
287 the sampled sedimentary units, or, in cases where sufficient published dates and stratigraphic information
288 were available, used PDFs of sediment unit boundaries (e.g. the boundary between subglacial till and
289 glacial-proximal sedimentary facies) generated with the OxCal P_Sequence deposition model^{63,64}. Outliers
290 were detected and dealt with using the default *general* outlier model in Oxcal⁷⁶ (Supplementary Figs. 7;8).
291 To account for possible deviations in R from the reconstructed Norwegian Sea ¹⁴C and Marine13, we
292 add a ΔR of 0 ± 50 ¹⁴C years (1σ) to each marine radiocarbon age determination. To calibrate marine
293 conventional ¹⁴C ages younger than 11800 ¹⁴C years, we use the Marine13 curve²⁹, terrestrial dates are
294 calibrated with the IntCal13²⁹.

295 For each phase of the deglaciation we outlined a succession of ice margins (Fig. 1) based on published
296 sediment core data, geomorphological interpretations and ice sheet reconstructions for the BSIS^{19,21,48,83–122}
297 and FIS^{19,42,47,72,73,80–82,111,123–136}. The available information is, however, too sparse to yield continuous
298 time-synchronous margins and we stress that the reconstructed margins are intended to capture the general
299 pattern of retreat rather than to be accurate representation of the ice sheet at a specific time. To account for
300 uncertainty in the ice sheet geometry, we follow the approach of¹⁹ and construct accompanying maximum
301 and minimum margins (Fig. 1). These are treated as the 95% quantiles. For margins derived from the
302 *Dated-1* reconstruction, we use their max and min margins¹⁹.

303 Ice sheet volume estimates

304 We converted the reconstructed ice sheet areas to volumes using the approximation proposed by Paterson³⁷:
305 $\log V = 1.23(\log S - 1)$, where V is volume and S is area. Paterson's formula was determined empirically
306 by regression of measurements on six extant ice sheets and ice caps, the boundary conditions of which
307 are not directly comparable to those of the EIS. To assess the sensitivity of the volume estimates to the
308 regression assumptions, we also used the area-volume relationships from the output of a recent ice-sheet
309 model of the EIS³⁸ to convert the reconstructed areas volume (Supplementary Fig. 9). Although the model-
310 based regression yields an EIS volume that is 2.7 m SLE smaller than the Paterson approximation at the
311 start of the deglaciation, the difference in the estimated ice loss between 14.7 and 14.4 kyr BP is only ~0.2
312 m SLE, which is negligible with respect to our conclusions (Supplementary Fig. 9). Paleo-depths of the
313 continental shelves on which the EIS was grounded are obscured by an unknown amount of isostatic uplift
314 since deglaciation. Without correcting for ice volume below flotation through glacio-isostatic modelling,
315 which is outside the scope of our study, our estimated volumes cannot be interpreted as eustatic sea-level
316 change. For each ice sheet margin reconstruction and associated uncertainty estimates, we generated a
317 PDF of the volume estimate using Gaussian kernels. The volume-PDF and accompanying age-PDF of each
318 reconstructed ice sheet were resampled using a Monte Carlo technique detailed at <https://github.com/kahaaga/EurasianDeglaciation>.
319

320 The effect of bioturbation

321 The Norwegian Sea sediment core GS07-148-17GC (Fig. 1) features a large, complex burrow with open
322 cavities containing pellets (Supplementary Fig. 5). Unlike ambient biogenic sediment mixing, which is
323 typically limited to an upper mixed layer, this burrow (or set of burrows) extends ~25 cm down into the
324 late HS1, and may have transported younger material down through this stratigraphic interval. Seven ¹⁴C
325 dates from this interval of the GS07-148-17GC core deviate from the ages in nearby cores GIK23074 and
326 HM79-6 (Fig. 1) at the same stratigraphic level. The presence of the large burrow through this interval
327 compelled us to discard these ¹⁴C dates from the ¹⁴C reconstruction (Supplementary Fig. 4).

328 To assess the potential impact of ambient biogenic sediment mixing on the observed decline in R at
329 the Bølling transition, we used the TURBO2 model¹³⁷, a mixed layer model with instantaneous mixing
330 designed to simulate the effects of bioturbation on proxy records from sedimentary particles such as
331 foraminifera. As input we used 1,024 simulated vectors of abundance generated as normally distributed
332 random values centered on the best-fit linear trend and with the standard deviation of the observed record
333 of the abundance of foraminifera from the MD95-2010 core³³. The simulated number of specimens picked
334 for measurement was set to 200. To focus on the change in R across the Bølling transition, we limited the
335 modeling to the time interval between ~15,400 and ~13,700 calendar yr BP. To keep the model as simple

336 as possible, we let the hypothetical true decline in R be an instantaneous step change superimposed on the
337 overall linear trend in the observed ^{14}C record, and we assumed a constant mixed layer depth. Under this
338 scenario, if we invoked a drop in the modeled R record of $\sim 1,220$ ^{14}C yr from 14,600 to 14,550 calendar yr
339 BP and used a mixed layer depth of 6 cm, then the bioturbated ^{14}C ages simulated by TURBO2 provided a
340 reasonable fit to the observed ^{14}C record (Supplementary Fig. 6). Hence, the effect of bioturbation would
341 be to temporally smear out a more abrupt event in the ^{14}C record. This smearing effect pushes the recalibrated
342 ^{14}C ages for the start of the deglaciation backwards in time, and attenuates the estimated EIS melt
343 water flux. An upward bias towards older ages affects ^{14}C dates between $\sim 13,200$ and $14,000$ ^{14}C yr BP in
344 particular, and is important to bear in mind if the ^{14}C record is to be used as a regional calibration curve.

345 Acknowledgements

346 This work is funded by the Research Council of Norway through grants no. 221999 (JB) and 231259 (BH),
347 and by the Bergen Research Foundation (BH). JB was also supported through the RISES project of the
348 Centre for Climate Dynamics at the Bjerknes Centre for Climate Research. Additional support was received
349 from JSPS KAKENHI 17H01168 and 15KK0151 (YY). JB, HH, KAH and BH acknowledge discussions
350 with colleagues at the department of Earth Science and the Bjerknes Centre for Climate Research at the
351 University of Bergen. We thank the captain and crew of R/V G.O. Sars for retrieving Core GS07-148-
352 17GC. Salad Yusuf Ali, Kristin Flesland and Eivind N. Støren is thanked for technical support.

353 Author contributions

354 J.B. conceived and designed the study, developed the core chronology, the deglaciation chronology, and
355 the ice margin reconstruction. H.H. collected sediment core GS07-148-17GC and performed tephrochronological
356 and geochemical analyses. Y. Y. performed AMS ^{14}C analyses. K. A. H. and J.B. developed the
357 Norwegian Sea ^{14}C reconstruction and performed statistical analyses. B. H. performed bioturbation modelling.
358 J.B., B.H. and K. A. H. wrote the paper, and all authors contributed to the writing of the final version
359 of the manuscript.

360 References

- 361 [1] Stocker, T. *Climate change 2013: the physical science basis: Working Group I contribution to the*
362 *Fifth assessment report of the Intergovernmental Panel on Climate Change* (Cambridge University
363 Press, 2014).
- 364 [2] Fairbanks, R. G. A 17,000-year glacio-eustatic sea level record: influence of glacial melting rates on
365 the Younger Dryas event and deep-ocean circulation. *Nature* **342**, 637–642 (1989).
- 366 [3] Blanchon, P. & Shaw, J. Reef drowning during the last deglaciation: Evidence for catastrophic
367 sea-level rise and ice-sheet collapse. *Geology* **23**, 4 (1995). URL [+http://dx.doi.org/10.1130/0091-7613\(1995\)023\(023\)3C0004:RDDTLD\(%\)3E2.3.CO;2](http://dx.doi.org/10.1130/0091-7613(1995)023(023)3C0004:RDDTLD(%)3E2.3.CO;2).
- 369 [4] Hanebuth, T., Statterger, K. & Grootes, P. M. Rapid flooding of the Sunda Shelf: a late-glacial
370 sea-level record. *Science* **288**, 1033–1035 (2000).
- 371 [5] Deschamps, P. *et al.* Ice-sheet collapse and sea-level rise at the Bolling warming 14,600 years ago.
372 *Nature* **483**, 559–564 (2012).
- 373 [6] Liu, J., Milne, G. A., Kopp, R. E., Clark, P. U. & Shennan, I. Sea-level constraints on the amplitude
374 and source distribution of meltwater pulse 1a. *Nature Geoscience* **9**, 130 (2016).
- 375 [7] Bassett, S. E., Milne, G. A., Mitrovica, J. X. & Clark, P. U. Ice sheet and solid earth influences on
376 far-field sea-level histories. *Science* **309**, 925–928 (2005).
- 377 [8] Clark, P. U. *et al.* Origin of the first global meltwater pulse following the last glacial maximum.
378 *Paleoceanography* **11**, 563–577 (1996).
- 379 [9] Clark, P. U., Mitrovica, J., Milne, G. & Tamisiea, M. Sea-level fingerprinting as a direct test for the
380 source of global meltwater pulse 1a. *Science* **295**, 2438–2441 (2002).

- 381 [10] Carlson, A. E. & Clark, P. U. Ice sheet sources of sea level rise and freshwater discharge
382 during the last deglaciation. *Reviews of Geophysics* **50** (2012). URL [https://agupubs.
onlinelibrary.wiley.com/doi/abs/10.1029/2011RG000371](https://agupubs.
383 onlinelibrary.wiley.com/doi/abs/10.1029/2011RG000371).
- 384 [11] McManus, J. F., Francois, R., Gherardi, J.-M., Keigwin, L. D. & Brown-Leger, S. Collapse and rapid
385 resumption of Atlantic meridional circulation linked to deglacial climate changes. *Nature* **428**, 834
386 (2004).
- 387 [12] Stanford, J., Rohling, E., Bacon, S. & Holliday, N. A review of the deep and surface currents around
388 eirik drift, south of greenland: Comparison of the past with the present. *Global and Planetary
389 Change* **79**, 244–254 (2011).
- 390 [13] Weertman, J. Stability of the junction of an ice sheet and an ice shelf. *Journal of Glaciology* **13**,
391 3–11 (1974).
- 392 [14] Mercer, J. H. West Antarctic ice sheet and CO₂ greenhouse effect: a threat of disaster. *Nature* **271**,
393 321 (1978).
- 394 [15] Hughes, T. J. The weak underbelly of the West Antarctic ice sheet. *Journal of Glaciology* **27**,
395 518–525 (1981).
- 396 [16] Joughin, I., Smith, B. E. & Medley, B. Marine ice sheet collapse potentially under way for the
397 Thwaites Glacier Basin, West Antarctica. *Science* **344**, 735–738 (2014).
- 398 [17] Ritz, C. *et al.* Potential sea-level rise from Antarctic ice-sheet instability constrained by observations.
399 *Nature* **528**, 115 (2015).
- 400 [18] DeConto, R. M. & Pollard, D. Contribution of Antarctica to past and future sea-level rise. *Nature*
401 **531**, 591 (2016).
- 402 [19] Hughes, A. L. C., Gyllencreutz, R., Lohne, Ø. S., Mangerud, J. & Svendsen, J. I. The last Eurasian
403 ice sheets – a chronological database and time-slice reconstruction, DATED-1. *Boreas* **45**, 1–45
404 (2016). URL <http://dx.doi.org/10.1111/bor.12142>.
- 405 [20] Stouffer, R. J. *et al.* Investigating the causes of the response of the thermohaline circulation to past
406 and future climate changes. *Journal of Climate* **19**, 1365–1387 (2006).
- 407 [21] Hormes, A., Gjermundsen, E. F. & Rasmussen, T. L. From mountain top to the deep sea—Deglaciation
408 in 4D of the northwestern Barents Sea ice sheet. *Quaternary Science Reviews* **75**, 78–99 (2013).
- 409 [22] Wang, Y. J. *et al.* A High-Resolution Absolute-Dated Late Pleistocene Monsoon Record from Hulu
410 Cave, China. *Science* **294**, 2345–2348 (2001). URL [http://science.sciencemag.org/
content/294/5550/2345](http://science.sciencemag.org/
411 content/294/5550/2345).
- 412 [23] Orland, I. J. *et al.* Direct measurements of deglacial monsoon strength in a Chinese stalagmite.
413 *Geology* **43**, 555 (2015). URL [+http://dx.doi.org/10.1130/G36612.1](http://dx.doi.org/10.1130/G36612.1).
- 414 [24] Cheng, H. *et al.* Ice Age Terminations. *Science* **326**, 248–252 (2009). URL [http://science.
sciencemag.org/content/326/5950/248](http://science.
415 sciencemag.org/content/326/5950/248).
- 416 [25] Deplazes, G. *et al.* Links between tropical rainfall and North Atlantic climate during the last glacial
417 period. *Nature Geoscience* **6**, 213 (2013).
- 418 [26] Hughen, K., Southon, J., Lehman, S., Bertrand, C. & Turnbull, J. Marine-derived ¹⁴C calibration
419 and activity record for the past 50,000 years updated from the Cariaco Basin. *Quaternary Science
420 Reviews* **25**, 3216–3227 (2006).
- 421 [27] Southon, J., Noronha, A. L., Cheng, H., Edwards, R. L. & Wang, Y. A high-resolution record of
422 atmospheric ¹⁴C based on Hulu Cave speleothem H82. *Quaternary Science Reviews* **33**, 32–41
423 (2012).
- 424 [28] Wu, J., Wang, Y., Cheng, H. & Edwards, L. R. An exceptionally strengthened East Asian summer
425 monsoon event between 19.9 and 17.1 ka BP recorded in a Hulu stalagmite. *Science in
426 China Series D: Earth Sciences* **52**, 360–368 (2009). URL [https://doi.org/10.1007/
s11430-009-0031-1](https://doi.org/10.1007/
427 s11430-009-0031-1).

- 428 [29] Reimer, P. J. *et al.* IntCal13 and Marine13 radiocarbon age calibration curves 0–50,000 years cal BP.
429 *Radiocarbon* **55**, 1869–1887 (2013).
- 430 [30] Seierstad, I. K. *et al.* Consistently dated records from the Greenland GRIP, GISP2 and NGRIP ice
431 cores for the past 104ka reveal regional millennial-scale $\delta^{18}\text{O}$ gradients with possible Heinrich event
432 imprint. *Quaternary Science Reviews* **106**, 29–46 (2014). URL <http://www.sciencedirect.com/science/article/pii/S027737911400434X>.
433
- 434 [31] Voelker, A. H. L. *Zur Deutung der Dansgaard-Oeschger Ereignisse in ultra-hochauflösenden*
435 *Sedimentprofilen aus dem Europäischen Nordmeer*. Ph.D. thesis, Institut für Geowissenschaften,
436 Christian-Albrechts-Universität (1999).
- 437 [32] Karpuz, N. K. & Jansen, E. A high-resolution diatom record of the last deglaciation from the SE
438 Norwegian Sea: Documentation of rapid climatic changes. *Paleoceanography* **7**, 499–520 (1992).
439 URL <http://dx.doi.org/10.1029/92PA01651>.
- 440 [33] Dokken, T. M. & Jansen, E. Rapid changes in the mechanism of ocean convection during the last
441 glacial period. *Nature* **401**, 458–461 (1999).
- 442 [34] Sarnthein, M., Balmer, S., Grootes, P. M. & Mudelsee, M. Planktic and benthic ^{14}C reservoir ages
443 for three ocean basins, calibrated by a suite of ^{14}C plateaus in the glacial-to-deglacial Suigetsu at-
444 mospheric ^{14}C record. *Radiocarbon* **57**, 129–151 (2015).
- 445 [35] Dreger, D. *Decadal to Centennial Scale Sediment Records of Ice Advance on the Barents Shelf and*
446 *Meltwater Discharge Into the Northeastern Norwegian Sea Over the Last 40 Kyr: Dekadische Bis*
447 *Jahrhundert-Variabilität Von Eisvorstößen Auf Dem Barentsschelf und Schmelzwasserschüben in Die*
448 *Nordöstliche Norwegensee Während Der Letzten 40 Ka*. Ph.D. thesis, Inst. für Geowiss. (1999).
- 449 [36] Sarnthein, M. *et al.* Fundamental modes and abrupt changes in North Atlantic circulation and climate
450 over the last 60 ky—Concepts, reconstruction and numerical modeling. In *The Northern North*
451 *Atlantic*, 365–410 (Springer, 2001).
- 452 [37] Paterson, W. S. B. Laurentide Ice Sheet: estimated volumes during late Wisconsin. *Reviews of*
453 *Geophysics* **10**, 885–917 (1972).
- 454 [38] Patton, H. *et al.* Deglaciation of the Eurasian ice sheet complex. *Quaternary Science Reviews* **169**,
455 148–172 (2017). URL <http://www.sciencedirect.com/science/article/pii/S0277379117302068>.
456
- 457 [39] Gregoire, L. J., Otto-Bliesner, B., Valdes, P. J. & Ivanovic, R. Abrupt bølling warming and ice saddle
458 collapse contributions to the meltwater pulse 1a rapid sea level rise. *Geophysical research letters* **43**,
459 9130–9137 (2016).
- 460 [40] Tarasov, L., Dyke, A. S., Neal, R. M. & Peltier, W. R. A data-calibrated distribution of deglacial
461 chronologies for the north american ice complex from glaciological modeling. *Earth and Planetary*
462 *Science Letters* **315**, 30–40 (2012).
- 463 [41] Shennan, I. *et al.* Relative sea-level changes, glacial isostatic modelling and ice-sheet reconstructions
464 from the british isles since the last glacial maximum. *Journal of Quaternary Science: Published for*
465 *the Quaternary Research Association* **21**, 585–599 (2006).
- 466 [42] Romundset, A., Bondevik, S. & Bennike, O. Postglacial uplift and relative sea level changes in
467 Finnmark, northern Norway. *Quaternary Science Reviews* **30**, 2398–2421 (2011).
- 468 [43] Lohne, Ø. S., Bondevik, S., Mangerud, J. & Svendsen, J. I. Sea-level fluctuations imply that the
469 younger dryas ice-sheet expansion in western norway commenced during the allerød. *Quaternary*
470 *Science Reviews* **26**, 2128–2151 (2007).
- 471 [44] Svendsen, J. I. & Mangerud, J. Late weichselian and holocene sea-level history for a cross-section
472 of western norway. *Journal of Quaternary Science* **2**, 113–132 (1987).
- 473 [45] Bentley, M. J. *et al.* A community-based geological reconstruction of antarctic ice sheet deglaciation
474 since the last glacial maximum. *Quaternary Science Reviews* **100**, 1–9 (2014).

- 475 [46] Buizert, C. *et al.* Greenland temperature response to climate forcing during the last deglaciation.
476 *Science* **345**, 1177–1180 (2014).
- 477 [47] Hafidason, H., Sejrup, H. P., Kristensen, D. K. & Johnsen, S. Coupled response of the late glacial
478 climatic shifts of northwest Europe reflected in Greenland ice cores: Evidence from the northern
479 North Sea. *Geology* **23**, 1059–1062 (1995).
- 480 [48] Rasmussen, T. L. *et al.* Paleoceanographic evolution of the SW Svalbard margin (76 N) since 20,000
481 ¹⁴C yr BP. *Quaternary Research* **67**, 100–114 (2007).
- 482 [49] Jenkins, A. *et al.* Observations beneath pine island glacier in west antarctica and implications for its
483 retreat. *Nature Geoscience* **3**, 468 (2010).
- 484 [50] Jacobs, S. S., Jenkins, A., Giulivi, C. F. & Dutrieux, P. Stronger ocean circulation and increased
485 melting under pine island glacier ice shelf. *Nature Geoscience* **4**, 519 (2011).
- 486 [51] Yokoyama, Y. *et al.* Widespread collapse of the ross ice shelf during the late holocene. *Proceedings*
487 *of the National Academy of Sciences* **113**, 2354–2359 (2016).
- 488 [52] Piasecka, E. D., Stokes, C. R., Winsborrow, M. C. & Andreassen, K. Relationship between mega-
489 scale glacial lineations and iceberg ploughmarks on the bjørnøyrenna palaeo-ice stream bed, barents
490 sea. *Marine Geology* **402**, 153–164 (2018).
- 491 [53] Pollard, D., DeConto, R. M. & Alley, R. B. Potential antarctic ice sheet retreat driven by hydrofrac-
492 turing and ice cliff failure. *Earth and Planetary Science Letters* **412**, 112–121 (2015).
- 493 [54] Wise, M. G., Dowdeswell, J. A., Jakobsson, M. & Larter, R. D. Evidence of marine ice-cliff insta-
494 bility in pine island bay from iceberg-keel plough marks. *Nature* **550**, 506 (2017).
- 495 [55] Howell, D., Siegert, M. J. & Dowdeswell, J. A. Modelling the influence of glacial isostasy on late
496 weichselian ice-sheet growth in the barents sea. *Journal of Quaternary Science: Published for the*
497 *Quaternary Research Association* **15**, 475–486 (2000).
- 498 [56] Edwards, T. L. *et al.* Revisiting antarctic ice loss due to marine ice-cliff instability. *Nature* **566**, 58
499 (2019).
- 500 [57] Ng, H. C. *et al.* Coherent deglacial changes in western atlantic ocean circulation. *Nature communi-*
501 *cations* **9** (2018).
- 502 [58] Condron, A. & Winsor, P. Meltwater routing and the younger dryas. *Proceedings of the National*
503 *Academy of Sciences* **109**, 19928–19933 (2012).
- 504 [59] Yokoyama, Y., Miyairi, Y., Matsuzaki, H. & Tsunomori, F. Relation between acid dissolution time
505 in the vacuum test tube and time required for graphitization for ams target preparation. *Nuclear*
506 *Instruments and Methods in Physics Research Section B: Beam Interactions with Materials and*
507 *Atoms* **259**, 330–334 (2007).
- 508 [60] Yokoyama, Y., Koizumi, M., Matsuzaki, H., Miyairi, Y. & Ohkouchi, N. Developing ultra small-scale
509 radiocarbon sample measurement at the university of tokyo. *Radiocarbon* **52**, 310–318 (2010).
- 510 [61] Yokoyama, Y. *et al.* A single stage accelerator mass spectrometry at the atmosphere and ocean
511 research institute, the university of tokyo. *Nuclear Instruments and Methods in Physics Research*
512 *Section B* (2018).
- 513 [62] Bronk Ramsey, C. Bayesian analysis of radiocarbon dates. *Radiocarbon* **51**, 337–360 (2009).
- 514 [63] Bronk Ramsey, C. Deposition models for chronological records. *Quaternary Science Reviews* **27**,
515 42–60 (2008).
- 516 [64] Bronk Ramsey, C. & Lee, S. Recent and planned developments of the program OxCal. *Radiocarbon*
517 **55**, 720–730 (2013).
- 518 [65] Rasmussen, T. L., van Weering, T. C. E. & Labeyrie, L. Climatic instability, ice sheets and ocean
519 dynamics at high northern latitudes during the last glacial period (58-10 KA BP). *Quaternary Science*
520 *Reviews* **16**, 71–80 (1997). URL [http://www.sciencedirect.com/science/article/
521 pii/S0277379196000455](http://www.sciencedirect.com/science/article/pii/S0277379196000455).

- 522 [66] Kissel, C. *et al.* Rapid climatic variations during marine isotopic stage 3: magnetic analysis
523 of sediments from Nordic Seas and North Atlantic. *Earth and Planetary Science Letters* **171**,
524 489–502 (1999). URL [http://www.sciencedirect.com/science/article/pii/
525 S0012821X99001624](http://www.sciencedirect.com/science/article/pii/S0012821X99001624).
- 526 [67] Ballini, M., Kissel, C., Colin, C. & Richter, T. Deep-water mass source and dynamic associated with
527 rapid climatic variations during the last glacial stage in the North Atlantic: A multiproxy investigation
528 of the detrital fraction of deep-sea sediments. *Geochemistry, Geophysics, Geosystems* **7**, n/a—n/a
529 (2006). URL <http://dx.doi.org/10.1029/2005GC001070>.
- 530 [68] Liu, Z. *et al.* Chinese cave records and the east asia summer monsoon. *Quaternary Science Reviews*
531 **83**, 115–128 (2014).
- 532 [69] Landais, A. *et al.* Ice core evidence for decoupling between midlatitude atmospheric water cycle and
533 greenland temperature during the last deglaciation. *Climate of the Past* **14**, 1405–1415 (2018).
- 534 [70] Andersen, K. K. *et al.* The greenland ice core chronology 2005, 15–42 ka. part 1: constructing the
535 time scale. *Quaternary Science Reviews* **25**, 3246–3257 (2006).
- 536 [71] Hjelstuen, B. O. *et al.* Late quaternary seismic stratigraphy and geological development of the south
537 vøring margin, norwegian sea. *Quaternary Science Reviews* **23**, 1847–1865 (2004).
- 538 [72] Lekens, W. A. H. *et al.* Laminated sediments preceding Heinrich event 1 in the Northern North
539 Sea and Southern Norwegian Sea: Origin, processes and regional linkage. *Marine Geology*
540 **216**, 27–50 (2005). URL [http://www.sciencedirect.com/science/article/pii/
541 S0025322704003585](http://www.sciencedirect.com/science/article/pii/S0025322704003585).
- 542 [73] Hjelstuen, B. O., Sejrup, H. P., Valvik, E. & Becker, L. W. M. Evidence of an ice-dammed lake
543 outburst in the North Sea during the last deglaciation. *Marine Geology* (2017).
- 544 [74] Rasmussen, S. O. *et al.* A new greenland ice core chronology for the last glacial termination. *Journal*
545 *of Geophysical Research: Atmospheres* **111** (2006).
- 546 [75] Bondevik, S., Mangerud, J., Birks, H. H., Gulliksen, S. & Reimer, P. Changes in North Atlantic
547 radiocarbon reservoir ages during the Allerød and Younger Dryas. *Science* **312**, 1514–1517 (2006).
- 548 [76] Bronk Ramsey, C. Dealing with outliers and offsets in radiocarbon dating. *Radiocarbon* **51**, 1023–
549 1045 (2009).
- 550 [77] Waelbroeck, C. *et al.* The timing of the last deglaciation in North Atlantic climate records. *Nature*
551 **412**, 724–727 (2001).
- 552 [78] Thornalley, D. J. R., McCave, I. N. & Elderfield, H. Tephra in deglacial ocean sediments south of
553 Iceland: Stratigraphy, geochemistry and oceanic reservoir ages. *Journal of Quaternary Science* **26**,
554 190–198 (2011). URL <http://dx.doi.org/10.1002/jqs.1442>.
- 555 [79] Stanford, J. D. *et al.* A new concept for the paleoceanographic evolution of Heinrich event 1 in
556 the North Atlantic. *Quaternary Science Reviews* **30**, 1047–1066 (2011). URL [http://www.
557 sciencedirect.com/science/article/pii/S0277379111000400](http://www.sciencedirect.com/science/article/pii/S0277379111000400).
- 558 [80] Dowdeswell, J. A., Ottesen, D., Evans, J., Cofaigh, C. Ó. & Anderson, J. B. Submarine glacial
559 landforms and rates of ice-stream collapse. *Geology* **36**, 819 (2008). URL [+http://dx.doi.
560 org/10.1130/G24808A.1](http://dx.doi.org/10.1130/G24808A.1).
- 561 [81] Rydningen, T. A., Vorren, T. O., Laberg, J. S. & Kolstad, V. The marine-based NW Fennoscandian
562 ice sheet: glacial and deglacial dynamics as reconstructed from submarine landforms. *Quaternary*
563 *Science Reviews* **68**, 126–141 (2013). URL [http://www.sciencedirect.com/science/
564 article/pii/S027737911300067X](http://www.sciencedirect.com/science/article/pii/S027737911300067X).
- 565 [82] Brendryen, J. *et al.* Ice sheet dynamics on the Lofoten–Vesterålen shelf, north Norway, from Late
566 MIS-3 to Heinrich Stadial 1. *Quaternary Science Reviews* **119**, 136–156 (2015). URL [http://
567 www.sciencedirect.com/science/article/pii/S0277379115001225](http://www.sciencedirect.com/science/article/pii/S0277379115001225).

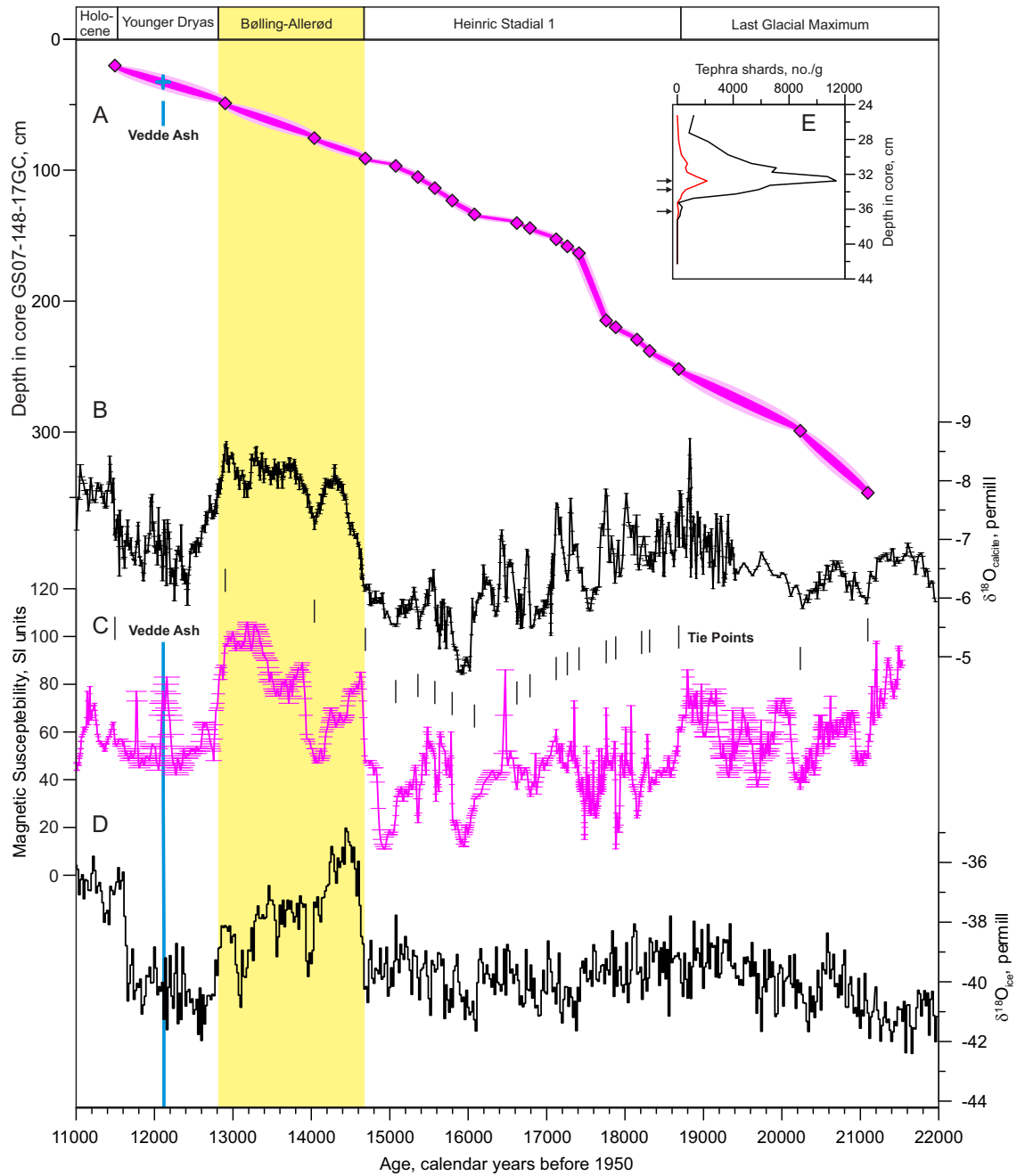
- 568 [83] Winsborrow, M. C. M., Andreassen, K., Corner, G. D. & Laberg, J. S. Deglaciation of a marine-
569 based ice sheet: Late Weichselian palaeo-ice dynamics and retreat in the southern Barents Sea
570 reconstructed from onshore and offshore glacial geomorphology. *Quaternary Science Reviews*
571 **29**, 424–442 (2010). URL [http://www.sciencedirect.com/science/article/pii/
572 S0277379109003333](http://www.sciencedirect.com/science/article/pii/S0277379109003333).
- 573 [84] Andreassen, K., Winsborrow, M. C. M., Bjarnadóttir, L. R. & Rüther, D. C. Ice stream retreat
574 dynamics inferred from an assemblage of landforms in the northern Barents Sea. *Quaternary Science
575 Reviews* **92**, 246–257 (2014).
- 576 [85] Bjarnadóttir, L. R., Winsborrow, M. C. M. & Andreassen, K. Deglaciation of the central Barents Sea.
577 *Quaternary Science Reviews* **92**, 208–226 (2014). URL [http://www.sciencedirect.com/
578 science/article/pii/S027737911300348X](http://www.sciencedirect.com/science/article/pii/S027737911300348X).
- 579 [86] Bjarnadóttir, L. R., Winsborrow, M. C. M. & Andreassen, K. Large subglacial meltwater features
580 in the central Barents Sea. *Geology* **45**, 159 (2017). URL [http://dx.doi.org/10.1130/
581 G38195.1](http://dx.doi.org/10.1130/G38195.1).
- 582 [87] Newton, A. M. W. & Huuse, M. Glacial geomorphology of the central Barents Sea: Implications for
583 the dynamic deglaciation of the Barents Sea Ice Sheet. *Marine Geology* **387**, 114–131 (2017). URL
584 <http://www.sciencedirect.com/science/article/pii/S0025322716302614>.
- 585 [88] Andreassen, K., Laberg, J. S. & Vorren, T. O. Seafloor geomorphology of the SW Barents Sea
586 and its glaci-dynamic implications. *Geomorphology* **97**, 157–177 (2008). URL [http://www.
587 sciencedirect.com/science/article/pii/S0169555X07002917](http://www.sciencedirect.com/science/article/pii/S0169555X07002917).
- 588 [89] Andreassen, K., Bjarnadóttir, L. R., Rüther, D. C. & Winsborrow, M. C. M. Retreat patterns and
589 dynamics of the former Bear Island Trough Ice Stream. *Geological Society, London, Memoirs* **46**,
590 445–452 (2016). URL <http://mem.lyellcollection.org/content/46/1/445>.
- 591 [90] Bartels, M. *et al.* Atlantic Water advection vs. glacier dynamics in northern Spitsbergen since early
592 deglaciation. *Climate of the Past* **13**, 1717–1749 (2017). URL [https://www.clim-past.
593 net/13/1717/2017/](https://www.clim-past.net/13/1717/2017/).
- 594 [91] Bjarnadóttir, L. R. & Andreassen, K. Ice-stream landform assemblage in Kveithola, western Barents
595 Sea margin. *Geological Society, London, Memoirs* **46**, 325–328 (2016). URL [http://mem.
596 lyellcollection.org/content/46/1/325](http://mem.lyellcollection.org/content/46/1/325).
- 597 [92] Bjarnadóttir, L. R., Rüther, D. C., Winsborrow, M. C. M. & Andreassen, K. Grounding-line dynamics
598 during the last deglaciation of Kveithola, W Barents Sea, as revealed by seabed geomorphology
599 and shallow seismic stratigraphy. *Boreas* **42**, 84–107 (2013). URL [http://dx.doi.org/10.
600 1111/j.1502-3885.2012.00273.x](http://dx.doi.org/10.1111/j.1502-3885.2012.00273.x).
- 601 [93] Bondevik, S., Mangerud, J., Ronnert, L. & Salvigsen, O. Postglacial sea-level history of Edgeøya
602 and Barentsøya, eastern Svalbard. *Polar Research* **14**, 153–180 (1995).
- 603 [94] Cadman, V. M. *Glacimarine sedimentation and environments during Late Weichselian and Holocene
604 in the Bellsund Trough and Van Keulenfjorden, Svalbard*. Ph.D. thesis, University of Cambridge
605 (1996).
- 606 [95] Esteves, M., Bjarnadóttir, L. R., Winsborrow, M. C. M., Shackleton, C. S. & Andreassen, K. Retreat
607 patterns and dynamics of the Sentralbankrenna glacial system, central Barents Sea. *Quaternary
608 Science Reviews* **169**, 131–147 (2017). URL [http://www.sciencedirect.com/science/
609 article/pii/S0277379117300550](http://www.sciencedirect.com/science/article/pii/S0277379117300550).
- 610 [96] Hald, M., Danielsen, T. K. & Lorentzen, S. Late Pleistocene-Holocene benthic foraminiferal
611 distribution in the southwestern Barents Sea: Paleoenviromental implications. *Boreas* **18**, 367–388
612 (1989).
- 613 [97] Hald, M. *et al.* Late-glacial and Holocene paleoceanography and sedimentary environments in the St.
614 Anna Trough, Eurasian Arctic Ocean margin. *Palaeogeography, Palaeoclimatology, Palaeoecology*
615 **146**, 229–249 (1999).

- 616 [98] Hogan, K. A. *et al.* Submarine landforms and ice-sheet flow in the Kvitøya Trough, northwestern
617 Barents Sea. *Quaternary Science Reviews* **29**, 3545–3562 (2010).
- 618 [99] Hogan, K. A. *et al.* Subglacial sediment pathways and deglacial chronology of the northern Bar-
619 ents Sea Ice Sheet. *Boreas* **46**, 750–771 (2017). URL <http://dx.doi.org/10.1111/bor.12248>.
620
- 621 [100] Jessen, S. P., Rasmussen, T. L., Nielsen, T. & Solheim, A. A new Late Weichselian and Holocene ma-
622 rine chronology for the western Svalbard slope 30,000–0 cal years BP. *Quaternary Science Reviews*
623 **29**, 1301–1312 (2010). URL [http://www.sciencedirect.com/science/article/
624 pii/S0277379110000521](http://www.sciencedirect.com/science/article/pii/S0277379110000521).
- 625 [101] Junttila, J., Aagaard-Sørensen, S., Husum, K. & Hald, M. Late Glacial–Holocene clay minerals
626 elucidating glacial history in the SW Barents Sea. *Marine Geology* **276**, 71–85 (2010).
- 627 [102] Knies, J., Kleiber, H.-P., Matthiessen, J., Müller, C. & Nowaczyk, N. Marine ice-rafted debris records
628 constrain maximum extent of Saalian and Weichselian ice-sheets along the northern Eurasian margin.
629 *Global and Planetary Change* **31**, 45–64 (2001).
- 630 [103] Kleiber, H. P., Knies, J. & Niessen, F. The Late Weichselian glaciation of the Franz Victoria Trough,
631 northern Barents Sea: ice sheet extent and timing. *Marine Geology* **168**, 25–44 (2000).
- 632 [104] Kristensen, D. K., Rasmussen, T. L. & Koç, N. Palaeoceanographic changes in the northern Barents
633 Sea during the last 16 000 years—new constraints on the last deglaciation of the Svalbard–Barents
634 Sea Ice Sheet. *Boreas* **42**, 798–813 (2013).
- 635 [105] Landvik, J. Y. *et al.* The last glacial maximum of Svalbard and the Barents Sea area: ice sheet extent
636 and configuration. *Quaternary Science Reviews* **17**, 43–75 (1998).
- 637 [106] Lantzsch, H. *et al.* Deglacial to Holocene history of ice-sheet retreat and bottom current strength
638 on the western Barents Sea shelf. *Quaternary Science Reviews* **173**, 40–57 (2017). URL [http://
639 www.sciencedirect.com/science/article/pii/S0277379117300525](http://www.sciencedirect.com/science/article/pii/S0277379117300525).
- 640 [107] Lubinski, D. J. *et al.* The last deglaciation of the Franz Victoria Trough, northern Barents Sea. *Boreas*
641 **25**, 89–100 (1996).
- 642 [108] Lubinski, D. J., Polyak, L. & Forman, S. L. Freshwater and Atlantic water inflows to the deep
643 northern Barents and Kara seas since ca 13 ¹⁴C ka: foraminifera and stable isotopes. *Quaternary
644 Science Reviews* **20**, 1851–1879 (2001).
- 645 [109] Lucchi, R. G. *et al.* Postglacial sedimentary processes on the Storfjorden and Kveithola trough
646 mouth fans: Significance of extreme glacimarine sedimentation. *Global and Planetary Change* **111**,
647 309–326 (2013). URL [http://www.sciencedirect.com/science/article/pii/
648 S0921818113002270](http://www.sciencedirect.com/science/article/pii/S0921818113002270).
- 649 [110] Nielsen, T. & Rasmussen, T. L. Reconstruction of ice sheet retreat after the last glacial maximum in
650 storfjorden, southern svalbard. *Marine Geology* **402**, 228–243 (2018).
- 651 [111] Ottesen, D., Dowdeswell, J. A. & Rise, L. Submarine landforms and the reconstruction of fast-
652 flowing ice streams within a large Quaternary ice sheet: The 2500-km-long Norwegian-Svalbard
653 margin (57°–80°N). *GSA Bulletin* **117**, 1033 (2005). URL [+http://dx.doi.org/10.1130/
654 B25577.1](http://dx.doi.org/10.1130/B25577.1).
- 655 [112] Patton, H. *et al.* Geophysical constraints on the dynamics and retreat of the Barents Sea ice sheet as a
656 paleobenchmark for models of marine ice sheet deglaciation. *Reviews of Geophysics* **53**, 1051–1098
657 (2015). URL <http://dx.doi.org/10.1002/2015RG000495>.
- 658 [113] Pau, M. & Hammer, Ø. Sedimentary environments in the south-western Barents Sea during the last
659 deglaciation and the Holocene: a case study outside the Ingøydjupet trough. *Polar Research* **35**,
660 23104 (2016). URL <https://doi.org/10.3402/polar.v35.23104>.
- 661 [114] Piasecka, E. D., Winsborrow, M. C. M., Andreassen, K. & Stokes, C. R. Reconstructing the retreat
662 dynamics of the Bjørnøyrenna Ice Stream based on new 3D seismic data from the central Barents
663 Sea. *Quaternary Science Reviews* **151**, 212–227 (2016). URL [http://www.sciencedirect.
664 com/science/article/pii/S027737911630347X](http://www.sciencedirect.com/science/article/pii/S027737911630347X).

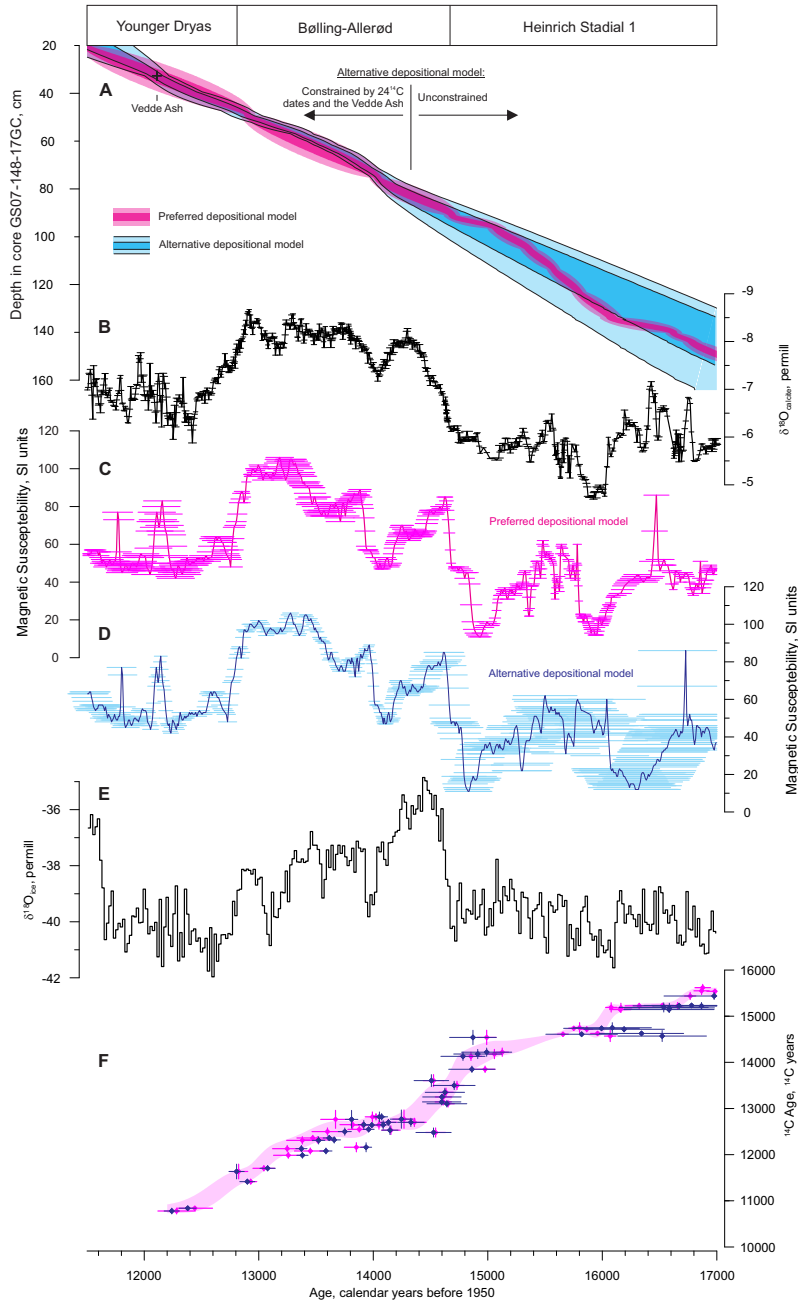
- 665 [115] Polyak, B., Lehman, S. J., Gataullin, V. & Jull, A. J. T. Two-step deglaciation of the southeastern
666 Barents Sea. *Geology* **23**, 567–571 (1995).
- 667 [116] R  ther, D. C., Mattingsdal, R., Andreassen, K., Forwick, M. & Husum, K. Seismic architecture
668 and sedimentology of a major grounding zone system deposited by the Bj  rn  yrenna Ice Stream
669 during Late Weichselian deglaciation. *Quaternary Science Reviews* **30**, 2776–2792 (2011). URL <http://www.sciencedirect.com/science/article/pii/S0277379111001831>.
670
- 671 [117] R  ther, D. C. *et al.* Pattern and timing of the northwestern Barents Sea Ice Sheet deglaciation and
672 indications of episodic Holocene deposition. *Boreas* **41**, 494–512 (2012). URL <http://dx.doi.org/10.1111/j.1502-3885.2011.00244.x>.
673
- 674 [118] R  ther, D. C., Winsborrow, M., Andreassen, K. & Forwick, M. Grounding line proximal sediment
675 characteristics at a marine-based, late-stage ice stream margin. *Journal of Quaternary Science* **32**,
676 463–474 (2017). URL <http://dx.doi.org/10.1002/jqs.2939>.
- 677 [119] Salvigsen, O. Radiocarbon dated raised beaches in Kong Karls Land, Svalbard, and their conse-
678 quences for the glacial history of the Barents Sea area. *Geografiska Annaler: Series A, Physical*
679 *Geography* **63**, 283–291 (1981).
- 680 [120]   lubowska-Woldengen, M. *et al.* Advection of Atlantic Water to the western and northern Svalbard
681 shelf since 17,500 calyr BP. *Quaternary Science Reviews* **26**, 463–478 (2007).
- 682 [121] Svendsen, J. I., Elverh  y, A. & Mangerud, J. The retreat of the Barents Sea Ice Sheet on the west-
683 ern Svalbard margin. *Boreas* **25**, 244–256 (1996). URL [http://dx.doi.org/10.1111/j.](http://dx.doi.org/10.1111/j.1502-3885.1996.tb00640.x)
684 [1502-3885.1996.tb00640.x](http://dx.doi.org/10.1111/j.1502-3885.1996.tb00640.x).
- 685 [122] Winsborrow, M. C. M., Stokes, C. R. & Andreassen, K. Ice-stream flow switching during deglacia-
686 tion of the southwestern Barents Sea. *GSA Bulletin* **124**, 275 (2012). URL [+http://dx.doi.org/10.1130/B30416.1](http://dx.doi.org/10.1130/B30416.1).
687
- 688 [123] Amundsen, H. B. *et al.* Late Weichselian–Holocene evolution of the high-latitude And  ya submarine
689 Canyon, north-Norwegian continental margin. *Marine Geology* **363**, 1–14 (2015).
- 690 [124] Bugge, T. *  vre lags geologi p   kontinentalsokkelen utenfor M  re og Tr  ndelag* (IKU, Institutt for
691 Kontinentalsokkelunders  kelser, 1980).
- 692 [125] Holtedahl, H. & Bjerkli, K. Late Quaternary sediments and stratigraphy on the continental shelf off
693 M  re-Tr  ndelag, W. Norway. *Marine Geology* **45**, 179205–202226 (1982).
- 694 [126] King, E. L., Haflidason, H., Sejrup, H. P. & L  vlie, R. Glacigenic debris flows on the North Sea
695 Trough Mouth Fan during ice stream maxima. *Marine Geology* **152**, 217–246 (1998). URL <http://www.sciencedirect.com/science/article/pii/S0025322798000723>.
696
- 697 [127] Laberg, J. S. *et al.* Late Quaternary palaeoenvironment and chronology in the Tr  nadjupet Slide area
698 offshore Norway. *Marine Geology* **188**, 35–60 (2002). URL <http://www.sciencedirect.com/science/article/pii/S0025322702002748>.
699
- 700 [128] Laberg, J. S., Eilertsen, R. S., Salomonsen, G. R. & Vorren, T. O. Submarine push moraine
701 formation during the early Fennoscandian Ice Sheet deglaciation. *Quaternary Research* **67**,
702 453–462 (2007). URL <http://www.sciencedirect.com/science/article/pii/S003358940700018X>.
703
- 704 [129] Laberg, J. S., Eilertsen, R. S. & Salomonsen, G. R. Deglacial dynamics of the Vestfjorden –
705 Tr  nadjupet palaeo-ice stream, northern Norway. *Boreas* **47**, 225–237 (2018). URL <http://dx.doi.org/10.1111/bor.12261>.
706
- 707 [130] Nyg  rd, A., Sejrup, H. P., Haflidason, H., Cecchi, M. & Ottesen, D. Deglaciation history of the
708 southwestern Fennoscandian Ice Sheet between 15 and 13 14C ka BP. *Boreas* **33**, 1–17 (2004).
- 709 [131] Nyg  rd, A. *et al.* Extreme sediment and ice discharge from marine-based ice streams: New evi-
710 dence from the North Sea. *Geology* **35**, 395 (2007). URL [+http://dx.doi.org/10.1130/G23364A.1](http://dx.doi.org/10.1130/G23364A.1).
711

- 712 [132] Rokoengen, K. & Bugge, T. Quaternary geology and deglaciation of the continental shelf off Troms,
713 north Norway. *Boreas* **8**, 217–227 (1979).
- 714 [133] Rokoengen, K. & Frengstad, B. Radiocarbon and seismic evidence of ice-sheet extent and the
715 last deglaciation on the mid-Norwegian continental shelf. *Norsk Geologisk Tidsskrift* **79**, 129–132
716 (1999).
- 717 [134] Sejrup, H. P., Nygård, A., Hall, A. M. & Hafliðason, H. Middle and Late Weichselian (Devensian)
718 glaciation history of south-western Norway, North Sea and eastern UK. *Quaternary Science Reviews*
719 **28**, 370–380 (2009). URL [http://www.sciencedirect.com/science/article/pii/
720 S0277379108002990](http://www.sciencedirect.com/science/article/pii/S0277379108002990).
- 721 [135] Vorren, T. O. & Kristoffersen, Y. Late Quaternary glaciation in the south-western Barents Sea.
722 *Boreas* **15**, 51–59 (1986). URL [http://dx.doi.org/10.1111/j.1502-3885.1986.
723 tb00742.x](http://dx.doi.org/10.1111/j.1502-3885.1986.tb00742.x).
- 724 [136] Vorren, T. O. & Plassen, L. Deglaciation and palaeoclimate of the Andfjord-Vågsfjord area, North
725 Norway. *Boreas* **31**, 97–125 (2002). URL [http://dx.doi.org/10.1111/j.1502-3885.
726 2002.tb01060.x](http://dx.doi.org/10.1111/j.1502-3885.2002.tb01060.x).
- 727 [137] Trauth, M. H. TURBO2: A MATLAB simulation to study the effects of bioturbation on paleoceanog-
728 raphic time series. *Computers & geosciences* **61**, 1–10 (2013).
- 729 [138] Sejrup, H. P., Clark, C. D. & Hjelstuen, B. O. Rapid ice sheet retreat triggered by ice stream debut-
730 tressing: Evidence from the North Sea. *Geology* **44**, 355–358 (2016).
- 731 [139] Becker, L. W., Sejrup, H. P., Hjelstuen, B. O., Hafliðason, H. & Dokken, T. M. Ocean-ice sheet
732 interaction along the se nordic seas margin from 35 to 15 ka bp. *Marine Geology* **402**, 99–117
733 (2018).
- 734 [140] Newton, A. J., Dugmore, A. J. & Gittings, B. M. Tephrobase: tephrochronology and the development
735 of a centralised european database. *Journal of Quaternary Science* **22**, 737–743 (2007).

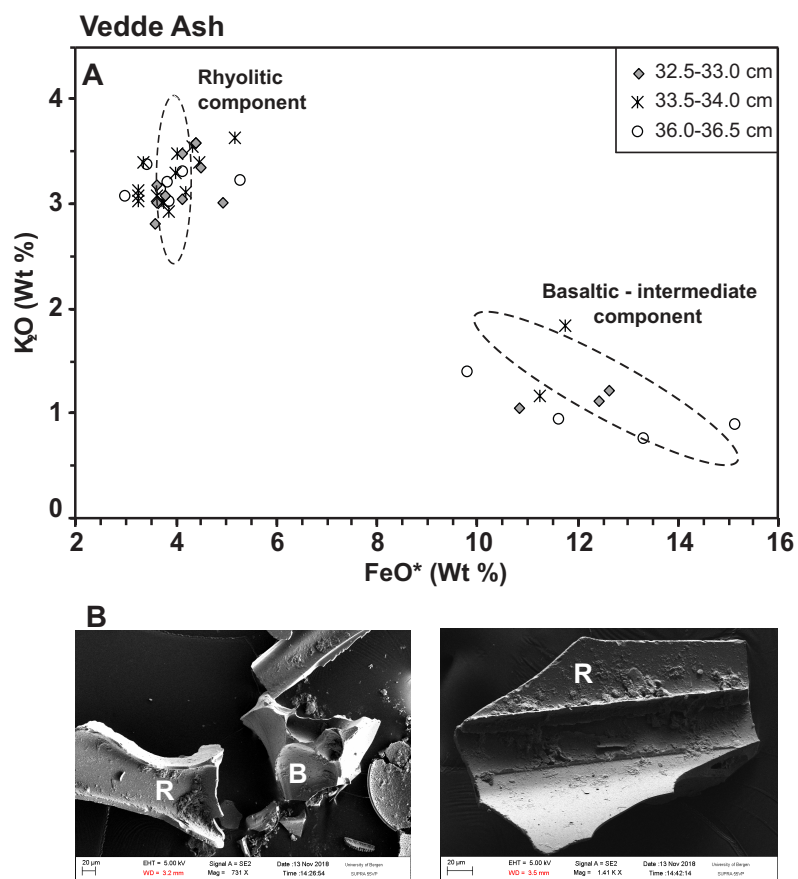
Supplementary Figures



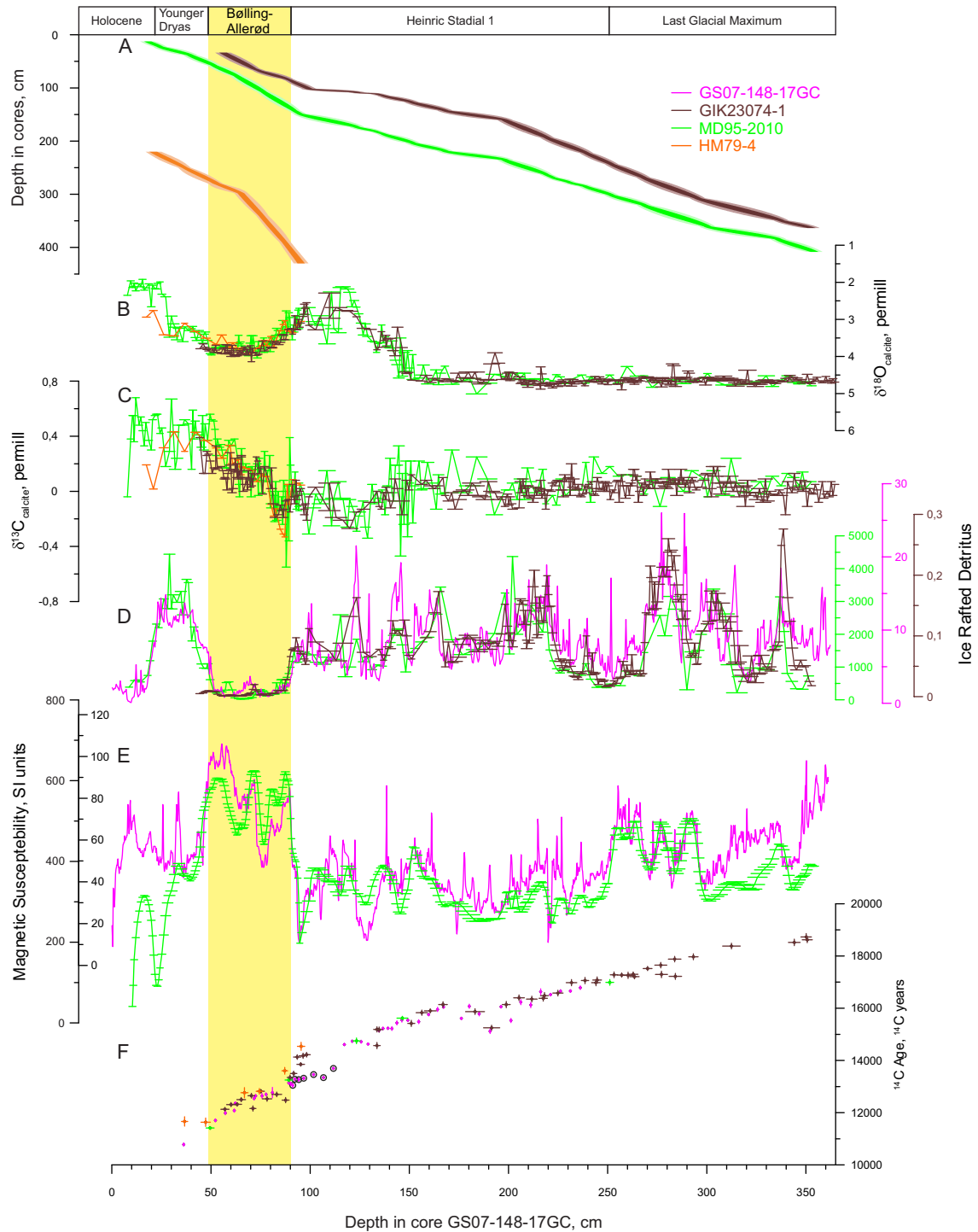
Supplementary Figure 1: Age-model of the Norwegian Sea core GS07-148-17GC. **A**, Age model constructed using the P_Sequence option in OxCal⁶³. The dark- and light-colored bands represent the respective 68.2% and 95.4% credible intervals of the model. The model is made by defining tie-points (diamonds and vertical dashes between **B**) and **(C)**) between the magnetic susceptibility record of core GS07-148-17GC (**C**) and the $\delta^{18}\text{O}$ record from Hulu cave (**B**)²⁷. While the Bølling transition is associated with high sedimentation rates and deposition of plumites closer to the continental shelf edge and the ice sheet grounding line^{82,100,109}, core GS07-148-17GC is located in a more distal setting where the direct influence from sediment-laden meltwater plumes is less likely. The interval with high sedimentation rates centered at about 17.5 kyr cal BP is related to the deposition of a plumite sourced from the Norwegian Channel Ice Stream^{71–73,138,139}. Horizontal error bars in **B–C** represent the 1σ uncertainty of the Oxcal-generated age-model for the respective records. **(D)**, The average of the $\delta^{18}\text{O}$ record from the Greenland summit ice cores (GISP2 and GRIP aligned on the GICC05 chronology³⁰), which is plotted for reference. The peak occurrence of the Vedde Ash in core GS07-148-17GC and the Greenland ice cores is indicated by the blue line. Note that the Vedde Ash has not been used to constrain the GS07-148-17GC chronology, yet the difference in the Vedde Ash ages is only 10 years. **E**, The distribution of tephra shards found in core GS07-148-17GC, including rhyolitic (black) and basaltic (red) shards. Arrows mark levels sampled for geochemical analyses of tephra shards (Supplementary Fig. 3).



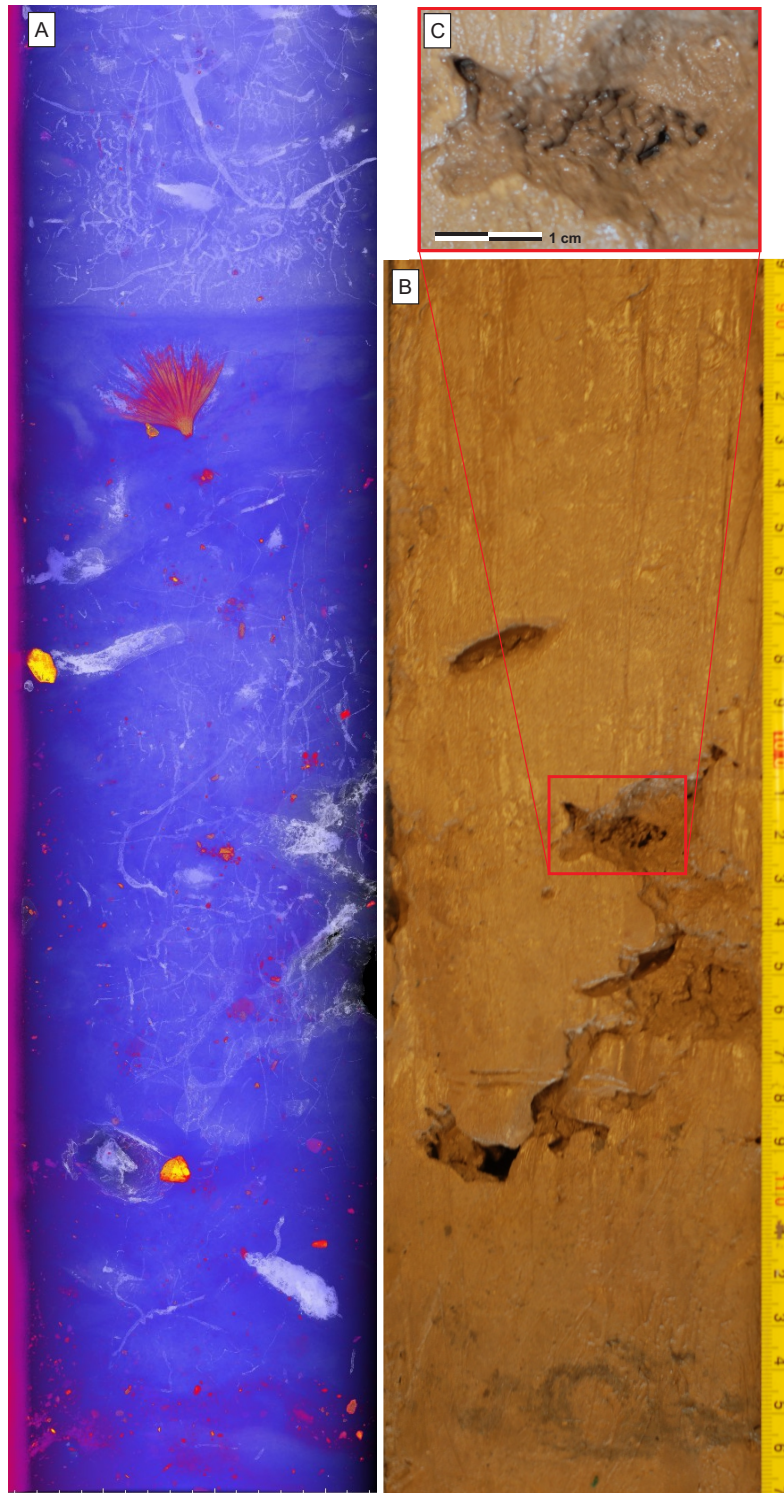
Supplementary Figure 2: Alternative depositional model of core GS07-148-17GC. **A**, comparison of the preferred deposition model (Magenta; Supplementary Fig. 1) and our alternative deposition model (cyan). Darker and lighter color represents the 68.2% and 95.4% credible intervals, respectively. The positions of the Vedde Ash, and the constrained and unconstrained segments of the models are indicated. **B**, The $\delta^{18}\text{O}$ record from Hulu cave as in Supplementary Fig. 1²⁷. **C-D**, the MS record of core GS07-148-17GC on the preferred (**C**, magenta) and alternative (**D**, blue) deposition model. The horizontal error bars in **B**, **C** and **D** represent the 1σ uncertainty of the Oxcal-generated deposition models for the respective records. **E**, the average of the $\delta^{18}\text{O}$ record from the Greenland summit ice cores (GISP2 and GRIP aligned on the GICC05 chronology³⁰) plotted for reference. **F**, the ^{14}C ages of the Norwegian Sea compilation plotted both on our preferred chronology (magenta) and the alternative chronology (blue), the light pink field is the Norwegian Sea ^{14}C reconstruction.



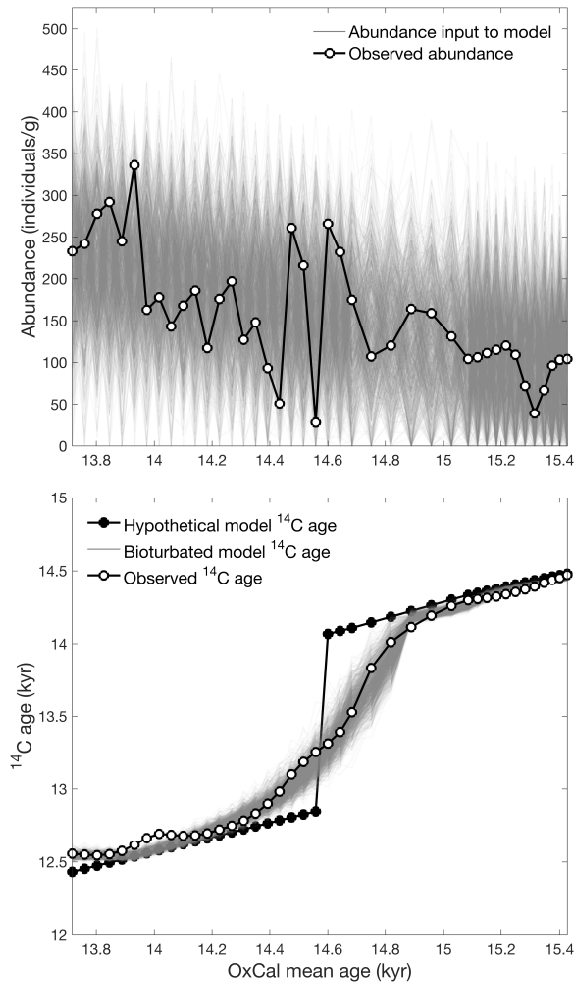
Supplementary Figure 3: The Vedde ash in core GS07-148-17GC. **A**, Bivariate plot of FeO^* vs K_2O showing the results from all the data presented in the Supplementary data File. All data are normalized to a 100% total on a water and volatile-free basis for data set comparison (the Supplementary Data File contains the original non-normalized geochemical data). Total iron is expressed as FeO^* . Compositional envelopes (dash lines) show the rhyolitic and basaltic-intermediate components of the Vedde Ash (from Tephabase: www.tephabase.org ¹⁴⁰). **B**, Scanning electron microscope images of glass shards from interval 32.5-33.0 cm depth in core GS07-148-17GC (B: basaltic glass, R: rhyolitic glass).



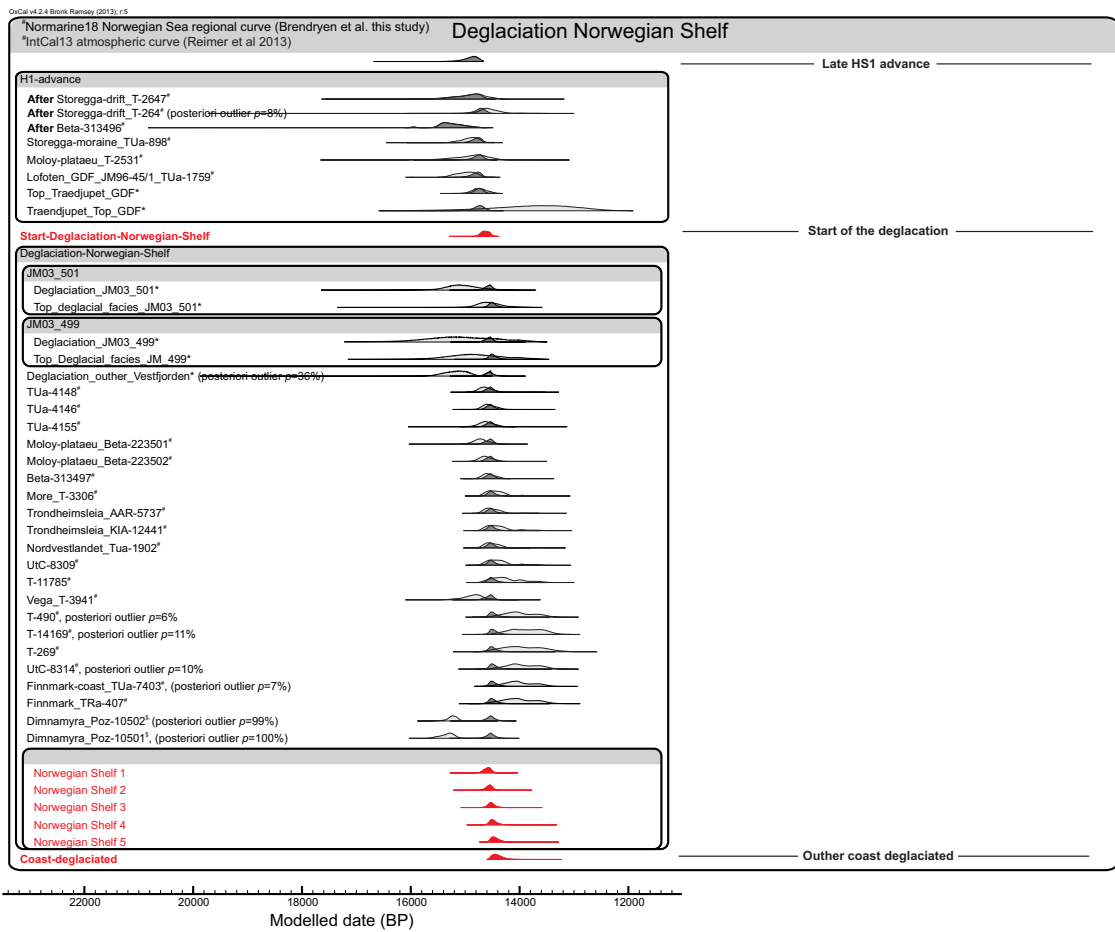
Supplementary Figure 4: Norwegian Sea data records plotted on GS07-148-17GC depth scale. **A**, Depth models of cores HM79-4, GIK23074-1 and MD95-2010 constructed using the P_Sequence option in OxCal⁶³. Light-colored uncertainty envelopes represent the 95.4% quantiles, while darker colored represent the 68.2% quantiles of the depth model PDF. The models are made by defining tie-point between the cores and core GS07-148-17GC using the records of **(B)** $\delta^{18}\text{O}^{31-33}$, **(C)** $\delta^{13}\text{C}^{31-33}$, **(D)** IRD^{31,33}, and **(E)** magnetic susceptibility³³. **F**, Compiled AMS $^{14}\text{C}^{31-34}$. Circles mark the dates that are excluded from further analysis due to distortion of the core stratigraphy from deep burrows (Supplementary Fig. 5). Horizontal error bars in **B-F** represent the 1σ uncertainty of the depth model for the respective cores.



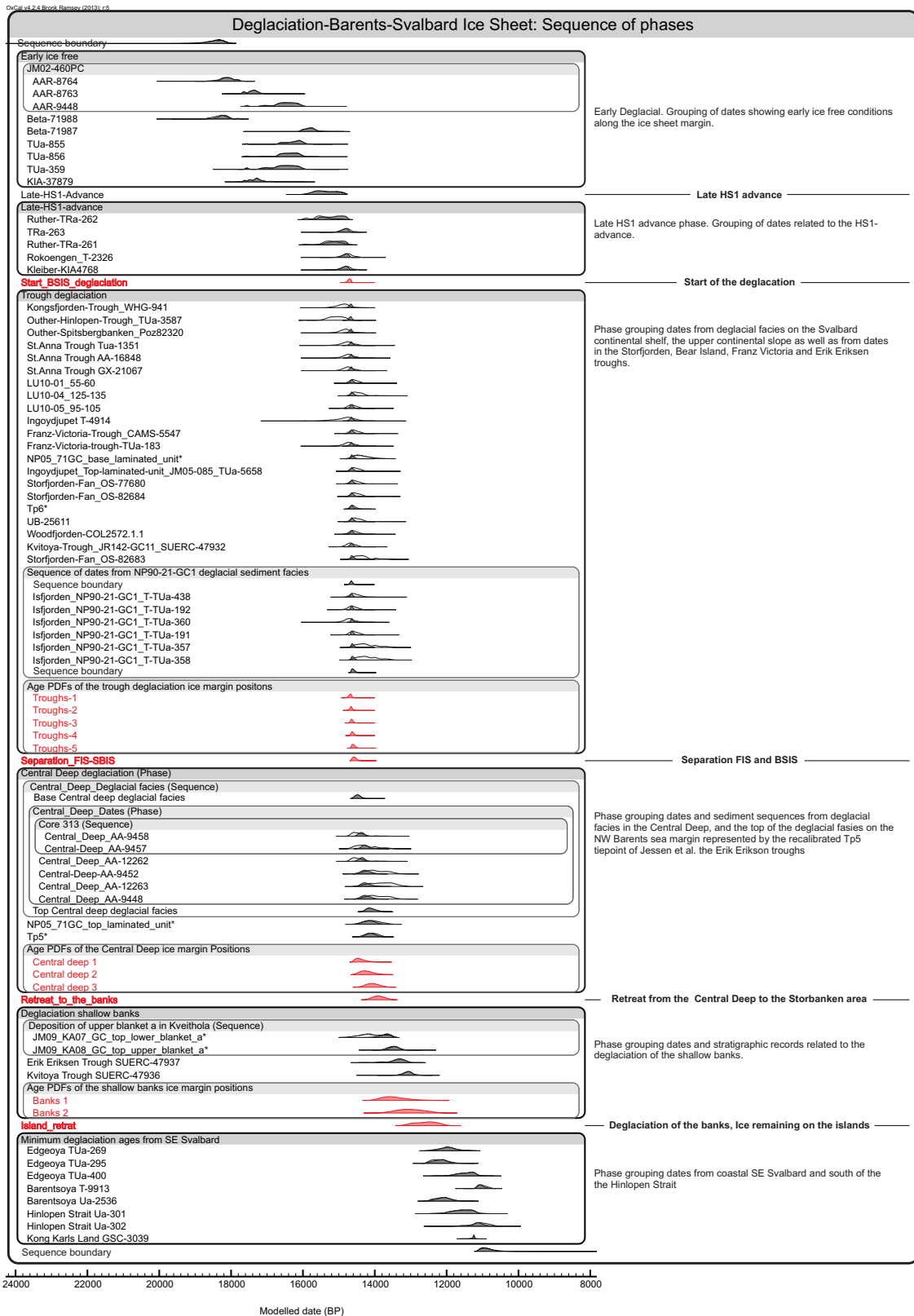
Supplementary Figure 5: Trace fossils and burrows between 83 and 117 cm depth in core GS07-148-17GC. **A**, Computed tomography radiograph with colour scheme chosen to emphasise trace fossils and burrows. White and light blue colours indicate low-density sediments and cavities, red and yellow colours mark high-density material. **B**, Photograph of the core surface showing open burrow tubes and cavities. **C**, Close-up of burrow cavity with ovoid pellets.



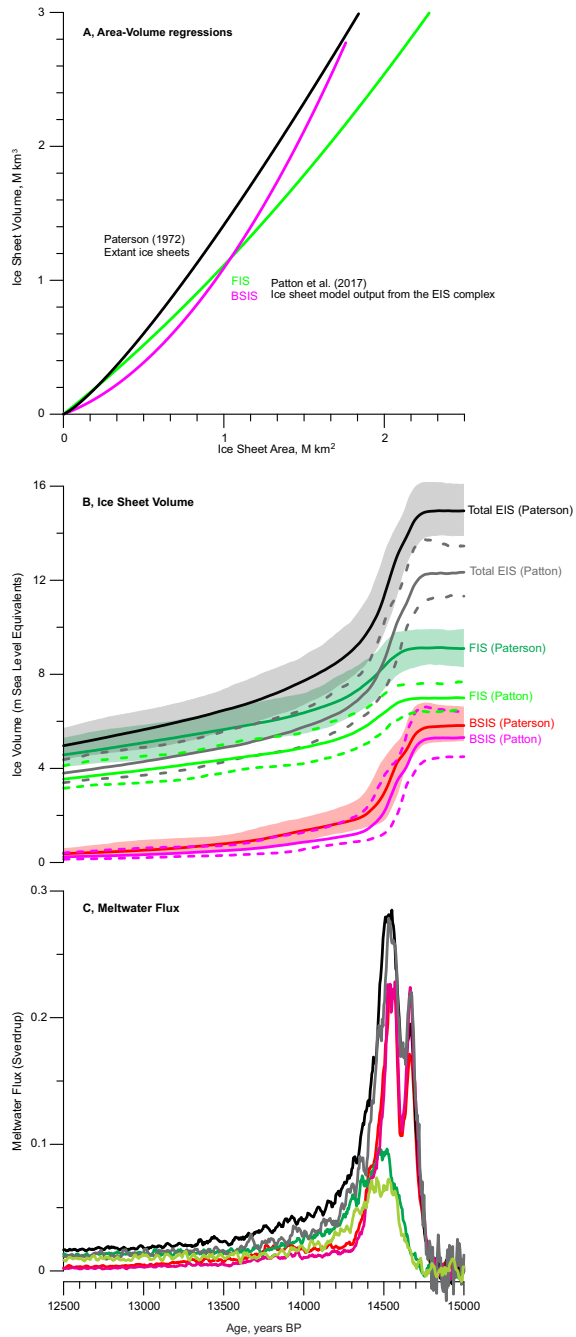
Supplementary Figure 6: The effect of bioturbation on the ^{14}C reconstruction at the Bølling transition. To assess the potential impact of bioturbation, we used the TURBO2 model¹³⁷ (Methods). As input we used 1,024 simulated abundance vectors (gray; top panel) generated as normally distributed random values centered on the best-fit linear trend and with the standard deviation of the observed abundance of foraminifera in core MD95-2210³³ (top panel). If we assume a constant mixed layer depth of 6 cm, then the observed change in ^{14}C age can be reproduced with reasonable accuracy in TURBO2 by invoking a hypothetical true ^{14}C age with an abrupt step change 14.56 kyr ago (lower panel). This result is not an attempt to infer the true ^{14}C age history, but rather to demonstrate that the effect of bioturbation would be to smear out the true event. As a consequence, our reconstruction is likely to overestimate the time scale of the EIS collapse and underestimate its contribution to the global MWP-1a.



Supplementary Figure 7: Bayesian deglacial chronology of the Norwegian continental shelf. As prior information, all radiocarbon dates or probability density functions of sediment unit boundaries are grouped into phases according to geographical and/or stratigraphical context. A phase in this context refers to a retreat (or advance) of the ice sheet in a specific area. The phases are ordered in a sequence following the relative chronological order. The PDF's of unmodeled conventional ^{14}C dates are calibrated using the new Norwegian Sea ^{14}C age reconstruction (Fig. 2) and is shown as light gray. Dark gray mark the modeled posteriori PDF of the same dates. Red PDF's show the posteriori age probabilities of undated events that corresponds to reconstructed ice margins depicted in Fig. (1).



Supplementary Figure 8: Bayesian deglacial chronology of the Barents-Svalbard ice sheet. As prior information, all radiocarbon dates or probability density functions of sediment unit boundaries are grouped into phases according to geographical and/or stratigraphical context. A phase in this context refers to a retreat (or advance) of the ice sheet in a specific area. The phases are ordered in a sequence following the relative chronological order. The PDF's of unmodeled conventional ^{14}C dates are calibrated using the new Norwegian Sea ^{14}C age reconstruction (Fig. 2) and is shown as light gray. Dark gray mark the modeled posteriori PDF of the same dates. Red PDF's show the posteriori age probabilities of undated events that corresponds to reconstructed ice margins depicted in Fig. (1).



Supplementary Figure 9: Comparison between area-volume regressions. **A**, Regression lines of ice sheet area and volume data used to convert the EIS area reconstruction to volume with the regression of³⁷ through six extant ice sheets (black) and regression lines (2nd order polynomial fits) through the EIS modeling output from³⁸ (green and purple). FIS, Fennoscandian Ice Sheet; BSIS, Barents Svalbard Ice Sheet; BHS, British Isles Ice Sheet. **B**, Comparison of the EIS volume estimated by the regression of³⁷ and a 2nd order polynomial regression of ice sheet specific area-volume output from a transient model simulation of the growth and decay of the EIS complex of³⁸. **C**, The corresponding meltwater fluxes. Color codes are the same as in **B**.